STUDY OF SOLID-STATE LASERS

Solid-state lasers are widely used in industry. It is inevitable that an equivalent thermal lens generated by the laser rod will be formed because of in-homogeneous heating of the rod. Also, the laser beam quality of solid-state lasers depends strongly on the pumping power due to the thermal lensing effect. This chapter covers three fields: (1) A new method is proposed to calculate the focal length of the thermal lens formed in the rod when the quality of the beam used for measurement is taken into account. A comparison is made between the thermal focal lengths calculated based on the proposed method and the conventional method. Experiments confirmed that the new equations provide better results than those predicted using the conventional equations; (2) Stability diagrams are presented to provide a clear understanding of the behaviour of a solid-state laser with a thermal lens. Particular emphasis is placed on finding optimal resonator configurations so that the beam size in the rod is stationary with respect to the thermal focal length; (3) Experiments were performed on a Q-switched Nd:YAG laser to evaluate the laser beam quality.

4.1 Introduction

As mentioned in the previous chapters, the solid-state laser is a widely used laser in laser material processing. Within the field of industrial laser material processing, the two most critical parameters are the focused spot size and beam intensity distribution on the workpiece, which are mainly determined by the laser resonator and related optical delivery systems. Therefore, the laser material processing quality depends mostly on the laser beam quality and the interaction between the laser beam and the processed material.

For solid-state lasers, the most important factor affecting the laser beam quality is the thermal lensing effects in the laser rods. Thermal lensing may produce transient effects, which cause unstable beam mode structure. The extent of the thermal lensing effect depends on the input power [4.1]. Various methods of compensation for spherical and non-spherical lensing effects and birefringence produced by the laser rod have been investigated to date [4.2].

In laser processing, the laser powers required by various applications are very different, in which the thermal lensing effects are also very different. The output power and beam divergence angle of solid-state lasers depend strongly on pumping power and duty cycle due to thermally induced lensing effect. It is necessary to know the resonator stability for different levels of thermal lensing effects. In this chapter, the thermal lensing effects, thermal lensing resonator stability, and laser beam quality of solid-state lasers will be investigated.

4.2 Investigation of Thermal Lensing Effects in Solid-state Lasers

4.2.1 Calculation and Measurement of Thermal Focal Length

The thermal focal length of a Nd: YAG rod can be measured in two steps. The first step is to pass a HeNe laser probe beam through a Nd:YAG rod with pumping switched off at ambient temperature. The beam propagation factor M^2 and other parameters could be measured by a laser beam diagnostic system as described in the previous chapter. The second step is to repeat the measurement with pumping switched on.

Assuming a perfect Nd:YAG rod, the beam propagation diagram without pumping is shown in Figure 4.1, where D_0 is the laser beam waist (in diameter) of the HeNe probe beam; Z_0 is the spacing between the laser beam waist and the assistant lens; and L_3 is the spacing between the assistant lens and the focused beam waist.

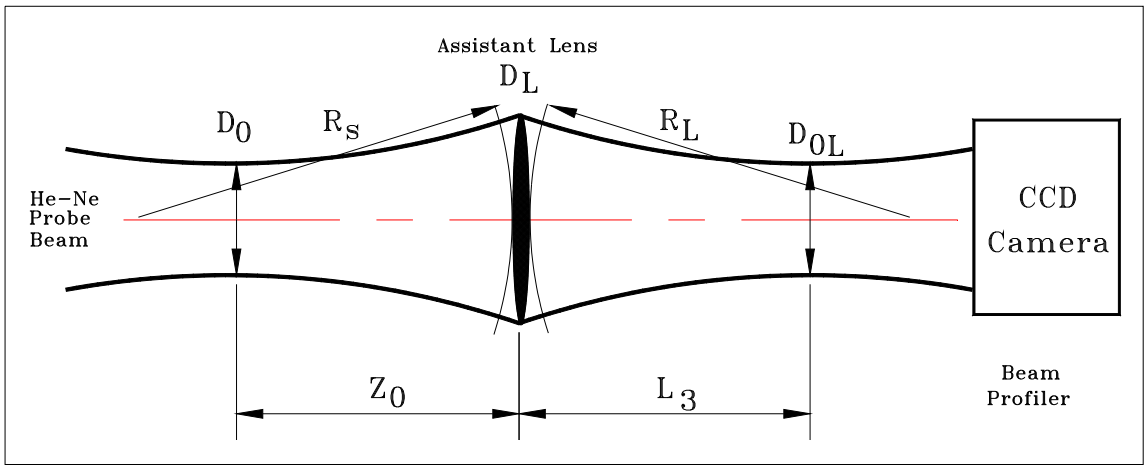

Figure 4.1 Beam propagation schematic diagram

The diameter of the HeNe laser beam at the assistant lens is given by [4.3]

$$D_L = D_{0L}\sqrt{1+\left(\frac{4\lambda M^2 L_3}{\pi D_{0L}^2}\right)^2} \tag{4.1}$$

where the beam propagation factor M^2, focused HeNe beam waist diameter D_{0L}, and the distance L_3 between the assistant lens and the beam waist focused by the lens are measured by a laser beam diagnostic system such as the Exitech system described in section 3.4. The laser wavelength, λ, is at 0.6328 μm.

The radii of curvature on the measurement side and on the source side of the assistant lens, R_L and R_S, are expressed, respectively as [4.3]

$$R_L = L_3\left[1+\left(\frac{\pi D_{0L}^2}{4\lambda M^2 L_3}\right)^2\right] \tag{4.2}$$

$$R_s = \frac{R_L F}{R_L - F} \tag{4.3}$$

where F is the focal length of the assistant lens.

The beam waist diameter D_0 and the beam waist location Z_0 with respect to the lens are calculated by [4.3]

$$D_0 = \frac{D_L}{\sqrt{1+\left(\frac{\pi D_L^2}{4\lambda M^2 R_S}\right)^2}} \tag{4.4}$$

and

$$Z_0 = \frac{R_S}{1+\left(\frac{4\lambda M^2 R_S}{\pi D_L^2}\right)^2} \tag{4.5}$$

When the Nd:YAG rod is pumped by a flashlamp, the equivalent measurement diagram is shown in Figure 4.2, where it is assumed that the equivalent thermal lens is at the centre of the Nd:YAG rod, the letter d represents the distance between the thermal lens and the assistant lens, D_0' is the focused beam waist diameter formed by the thermal lens, and D_{0L}' is the focused beam waist diameter formed by the combined effects of the two lenses. The parameters Z_0' and D_0' can be obtained from Equations (4.1) - (4.5).

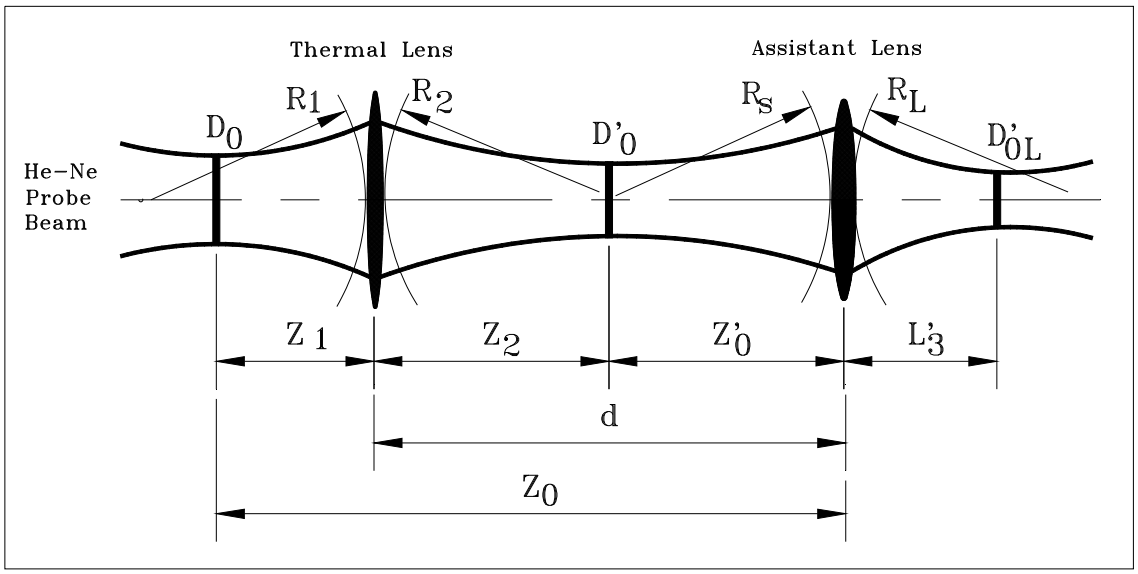

Figure 4.2 Schematic diagram of measuring thermal lens

The radius of curvature on the right side of the equivalent thermal lens due to the Nd:YAG rod, R_2, is given by

$$R_2 = Z_2\left[1+\left(\frac{\pi D_0'^2}{4\lambda M^2 Z_2}\right)^2\right] \tag{4.6}$$

where $Z_2 = d - Z_0'$, and the radius of curvature on the left side of the equivalent thermal lens, R_1, is given by

$$R_1 = Z_1\left[1+\left(\frac{\pi D_0^2}{4\lambda M^2 Z_1}\right)^2\right] \tag{4.7}$$

where $Z_1 = Z_0 - d$.

The relationship between the radii of curvature of the wavefronts and the focal length of a thin lens is well known as

$$\frac{1}{f} = \frac{1}{R_1} + \frac{1}{R_2} \tag{4.8}$$

where f is the focal length of the thermal lens caused by the Nd:YAG rod. The radius R_1 or R_2 is taken to be positive if it is convex. Therefore

$$f_1 = \frac{R_1 R_2}{R_1 + R_2} \tag{4.9}$$

where f_1 is the focal length of the thermal lens calculated by the proposed method.

In the conventional method of measuring thermal focal length of a Nd:YAG rod, a collimated HeNe laser beam is focused by the pumped rod. The distance between the centre of the rod and the minimum spot is considered as the thermal focal length. This method is simple but not accurate enough since there is a bi-focusing effect of the rod owing to birefringence. In order to improve the measurement accuracy, an assistant focusing lens and a beam expander are used as shown in Figure 4.3. The beam minimum spot going through the rod and the assistant lens is considered as the focus G formed jointly by the thermal lens and the assistant lens. Based on geometrical optics, the focal length of the thermal lens, f_2, is given by [4.4]

$$f_2 = d + \frac{FL_3'}{F - L_3'} \tag{4.10}$$

where d is the distance between the thermal lens and the assistant lens (here $d = 935$ mm), F is the focal length of the assistant lens (here $F = 133$ mm), and L_3' is the distance between the assistant lens and the focus G.

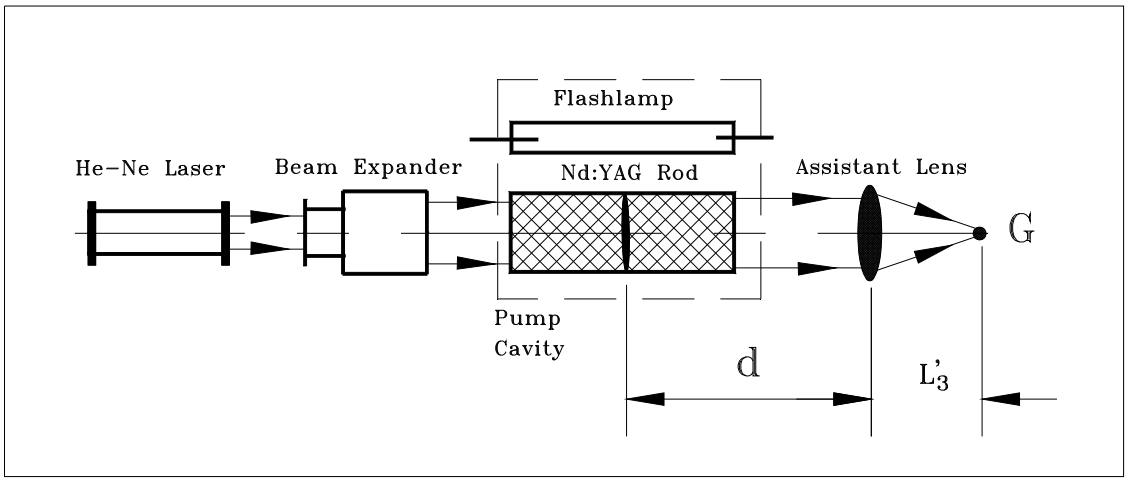

Figure 4.3 Schematic diagram of measuring thermal lens for the conventional method

The effects of using Equation (4.9) and Equation (4.10) will be compared based on the following expression

$$\delta = \frac{f_2 - f_1}{f_1} \times 100\% \qquad (4.11)$$

where δ is defined as difference percentage between the two methods.

4.2.2 Experimental Set-up

Experiments were performed on the NEC M690B Nd:YAG laser system. The size of the Nd:YAG rod used was ϕ4×100 mm. The YAG rod was pumped by a CW flashlamp with electrical power from 0 to 5 kW. The light source used to measure the thermal effects in the Nd:YAG rod was a HeNe laser beam. A 2× beam expander was used for more precise measurements. The Exitech laser beam diagnostic system was employed. The block diagram is shown in Figure 4.4.

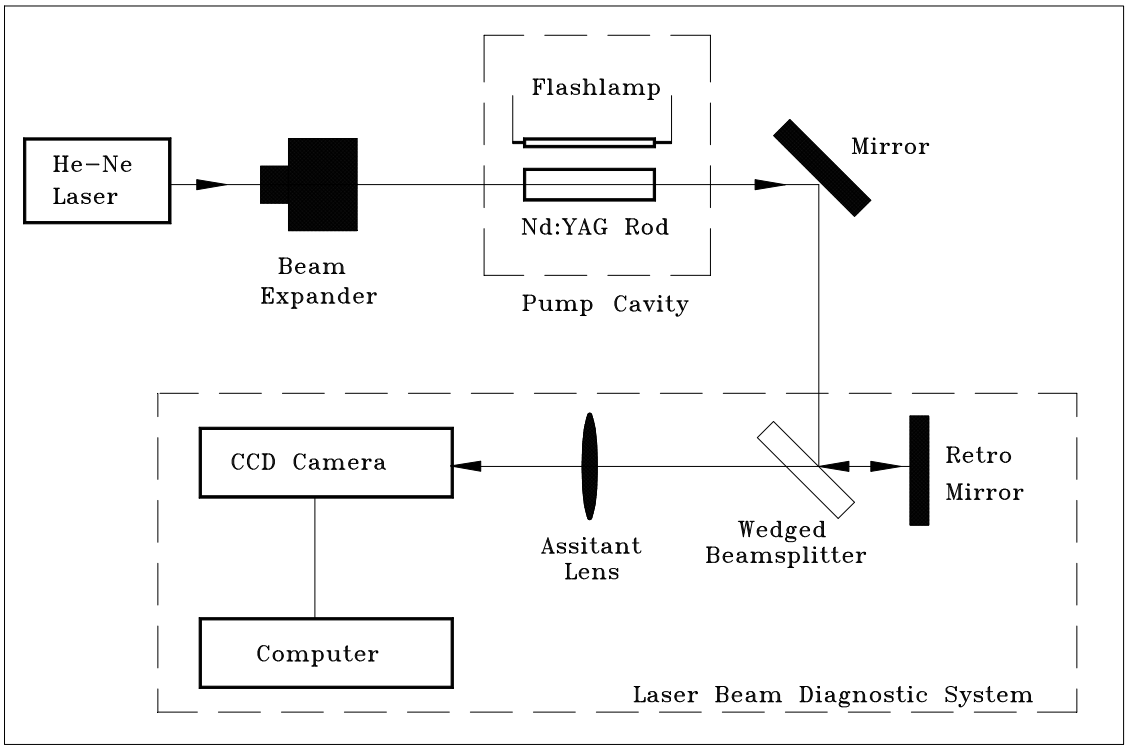

Figure 4.4 Experimental set-up for measuring thermal focal length

4.2.3 Beam Parameters of HeNe Laser Used

At first, the beam parameters of the HeNe laser were measured without pumping the Nd:YAG rod. The beam waist (D_0), divergence angle (full angle), and beam waist location with respect to the assistant lens (Z_0) were measured and shown in Table 4.1. Beam II was obtained from Beam I via a beam expander. Beam I has a beam waist diameter of 1.83 mm, and Beam II has a beam waist diameter of 2.57 mm. Figure 4.5 shows a focused beam propagation parameters given by the Exitech beam diagnostic system. The experiments showed that the beam waist was not located at the focal plane of the assistant lens. However, the beam intensity profile at the waist is the same as that at the focus since the lens Fresnel number is greater than 10 [4.5].

Table 4.1 HeNe laser beam parameters measured

	Beam I	Beam II
Beam propagation factor, M^2	4.82	5.41
Beam waist diameter, D_0, mm	1.83	2.57
Beam diameter at the rod, mm	1.89	2.61
Divergence angle, θ, mrad	2.12	1.70
Beam waist location, Z_0, mm	1201	729

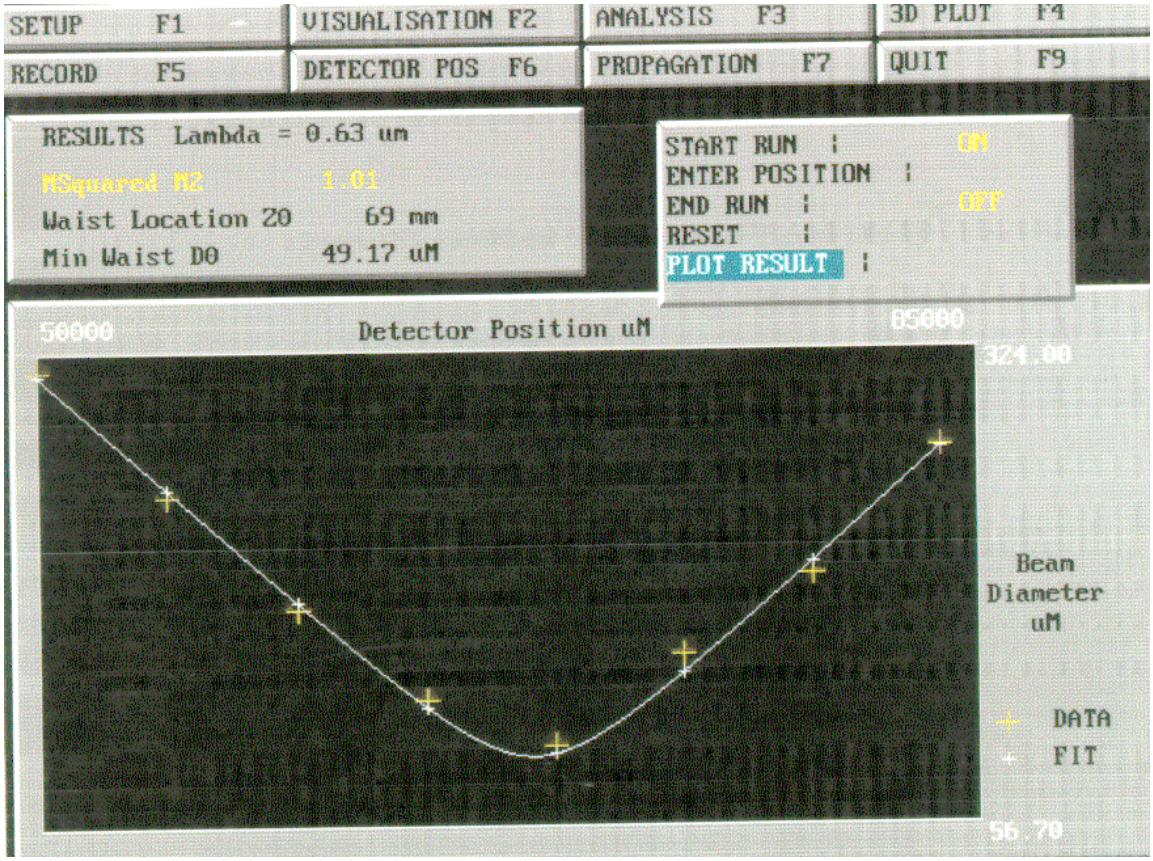

Figure 4.5 Focused beam propagation parameters given by the beam diagnostic system

4.2.4 Measured Thermal Focal Length

The measured relevant parameters and calculated thermal focal lengths are shown in Table 4.2 and Figure 4.6, where L_3' and D_{0L}' are the dimensions indicated in Figure 4.2, and M^2 is the beam propagation factor of the HeNe laser going through the Nd:YAG rod. The thermal focal lengths, f_1 (using the new equation) and f_2 (using the conventional equation), are calculated using Equations (4.9) and (4.10), respectively. δ is calculated with Equation (4.11). The input power of 2.93 kW is the approximate threshold for operating the YAG laser.

Table 4.2 Measured relevant parameters and calculated thermal focal lengths

Pumping power (kW)		2.93	3.13	3.22	3.40	3.56	3.71	3.90	4.06
Beam I	L_3' (mm)	178	179	177	173	172	170	169	169
	D_{0L}' (μm)	194	189	187	168	188	199	200	211
	M^2	1.64	1.84	2.06	2.21	2.68	3.23	3.65	4.43

	f_1 (mm)	568	538	515	465	470	456	435	419
	f_2 (mm)	409	417	400	360	348	324	311	311
	δ(%)	-28.0	-22.4	-22.4	-22.7	-25.9	-29.0	-28.6	-25.9
Beam II	L_3' (mm)	178	179	178	179	175	172	171	168
	D_{0L}' (μm)	230	223	221	196	176	172	183	192
	M^2	2.70	2.81	3.08	3.09	3.27	3.76	4.41	4.65
	f_1 (mm)	560	541	522	492	444	409	407	389
	f_2 (mm)	409	417	409	417	381	348	337	297
	δ(%)	-26.9	-22.9	-21.7	-15.1	-14.3	-14.9	-17.3	-23.7

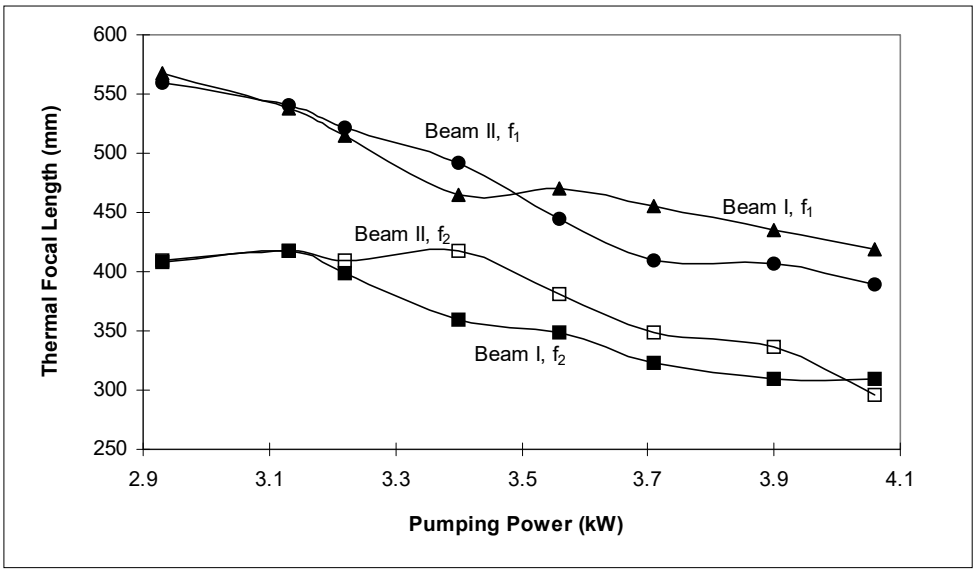

Figure 4.6 Thermal focal length vs. pumping power

4.2.5 Discussions

As shown in Table 4.2, the difference in the thermal focal lengths calculated by the two methods ranges from 14.3% to 29.0%. This is because Equation (4.11) is simplified according to geometrical optics and the focal position is often not where the smallest spot is [4.6, 4.7]. Now let us consider the role of a thin focusing lens in the transformation of a Gaussian beam, as shown in Figure 4.7.

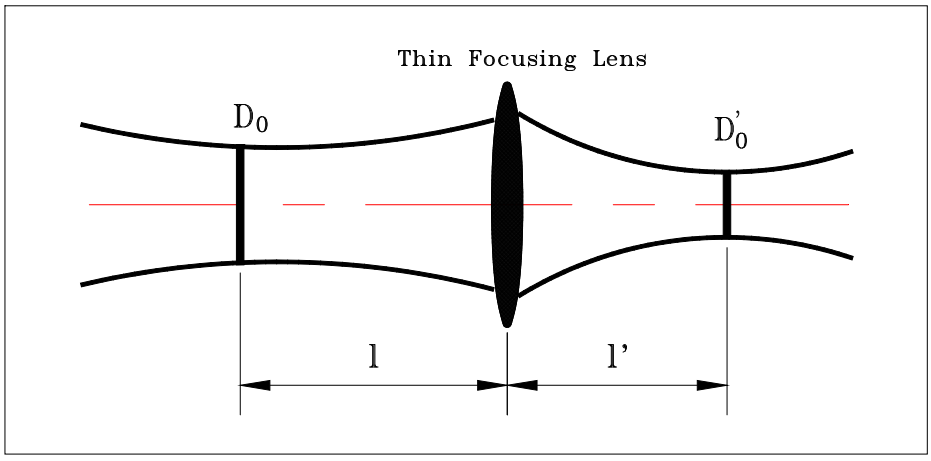

Figure 4.7 Gaussian beam transformation by a thin focusing lens

Assume that a Gaussian beam with a beam waist D_0 ($D_0=2\omega_0$) goes through a thin focusing lens, the location of a new beam waist D_0' at a distance l' is given by [4.8]

$$l' = F + \frac{(l-F)F^2}{(l-F)^2 + \left(\frac{\pi D_0^2}{4\lambda}\right)^2} \qquad (4.12)$$

where F is the focal length of the thin focusing lens, and l is the distance between the beam waist D_0 and the thin focusing lens. If

$$\left(\frac{\pi D_0^2}{4\lambda}\right)^2 << (l-F)^2 \tag{4.13}$$

Equation (4.12) becomes

$$l' = F + \frac{F^2}{l-F} = \frac{lF}{l-F} \tag{4.14}$$

that is,

$$\frac{1}{l'} + \frac{1}{l} = \frac{1}{F} \tag{4.15}$$

Equation (4.15) is the same as the imaging formula in geometrical optics. This means that Gaussian beam transformation can be treated using geometrical optics if the distance between the beam waist and the rear focus of the focusing lens is sufficiently large.

Thus, the difference percentage (δ) is theoretically defined as

$$\delta = \frac{l_1 - l_2}{l_1} \tag{4.16}$$

where
$$l_1 = F + \frac{(l-F)F^2}{(l-F)^2 + \left(\frac{\pi D_0^2}{4\lambda}\right)^2} \tag{4.17}$$

and

$$l_2 = \frac{lF}{l-F} \tag{4.18}$$

Now we proceed to check whether Equation (4.13) is satisfied in our experiments. The schematic diagram of the combination of the thermal lens and the assistant lens is shown in Figure 4.8, where $f_t' = -f_t$, $f_a' = -f_a$, and $F' = -F$.

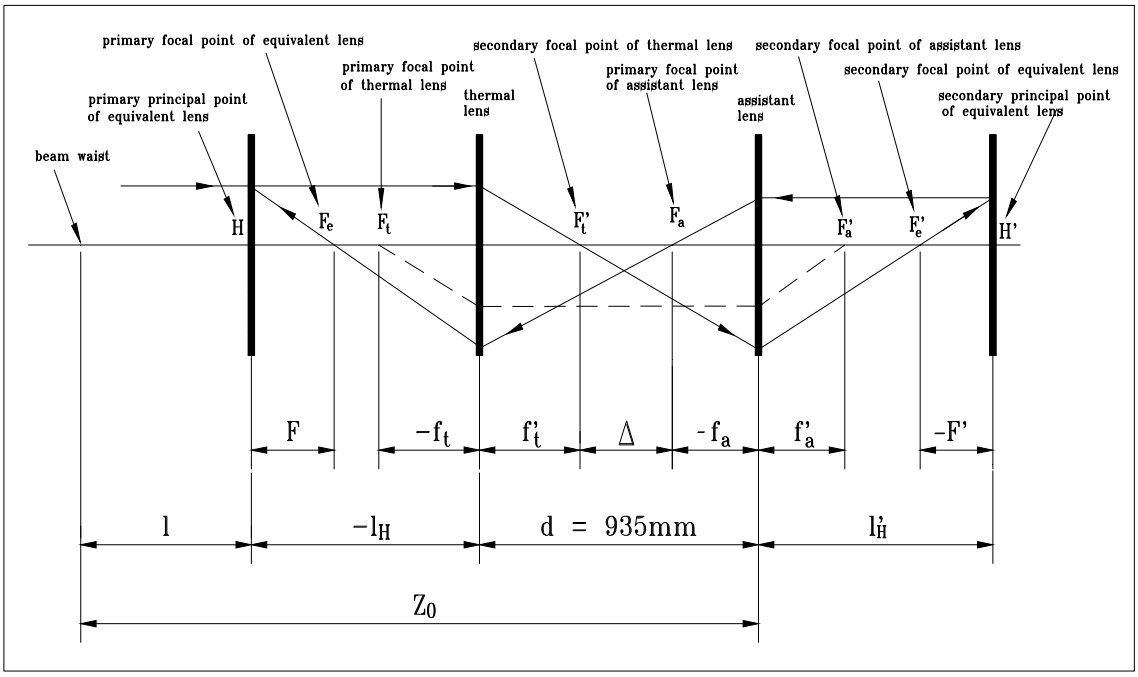

Figure 4.8 Schematic diagram of the combination of two lenses

The equivalent focal length of the thermal lens and the assistant lens, *F'*, and the distance between the primary principal point of the equivalent lens and the thermal lens, l_H, are given by [4.9]

$$F' = -F = \frac{f_a' f_t'}{f_a' + f_t' - d} \tag{4.19}$$

and

$$-l_H = F' \frac{d}{f_a} \tag{4.20}$$

From Figure 4.8, the distance between the beam diameter D_0 and the primary principal point of the equivalent lens, *l*, is given by

$$l = Z_0 - d + l_H \tag{4.21}$$

Therefore, using Equation 4.16, the calculated equivalent focal length F' should fall between 79 mm to 395 mm since the approximate range of thermal focal length measured is from 300 mm to 600 mm. The actual parameters determined in the experiments with respect to Equation (4.13) are shown in Table 4.3.

Table 4.3 Actual parameters with respect to Equation (4.13)

	Beam I	Beam II
$\left(\pi\omega_0^2/\lambda\right)^2$	4152^2	8130^2
$(l-F)^2$	368^2 @ F = 79mm 2908^2 @ F = 395mm	840^2 @ F = 79mm 3377^2 @ F = 395mm

It is clear from Table 4.3 that Equation (4.13) is not satisfied. Therefore the calculations based on Equation (4.9) are more reasonable than those based on Equation (4.10). Using Equations (4.16) - (4.18) and Table 4.3, the theoretical values of the δ's range between -8.9% to -21.5%.

In order to confirm the conclusion stated above and examine experimental repeatability, more experiments were carried out. The average focal lengths and the standard deviations corresponding to the proposed and the conventional methods are shown in Figure 4.9, The standard deviation is a measure of how widely values are dispersed from the average value (the mean). It uses the following formula [4.10]

$$STDEV = \sqrt{\frac{n\sum x^2 - \left(\sum x\right)^2}{n(n-1)}} \qquad (4.22)$$

where x is the focal length values and n is the number of experiments (here $n = 4$).

It could be concluded from Figure 4.9 that the standard deviation for the proposed method is smaller than that for the conventional method. Also, as will be shown later, the resonators with the focal lengths calculated from the proposed method are stable, but those with the focal lengths calculated from the conventional method are unstable. This also indicates that the proposed method is more reliable.

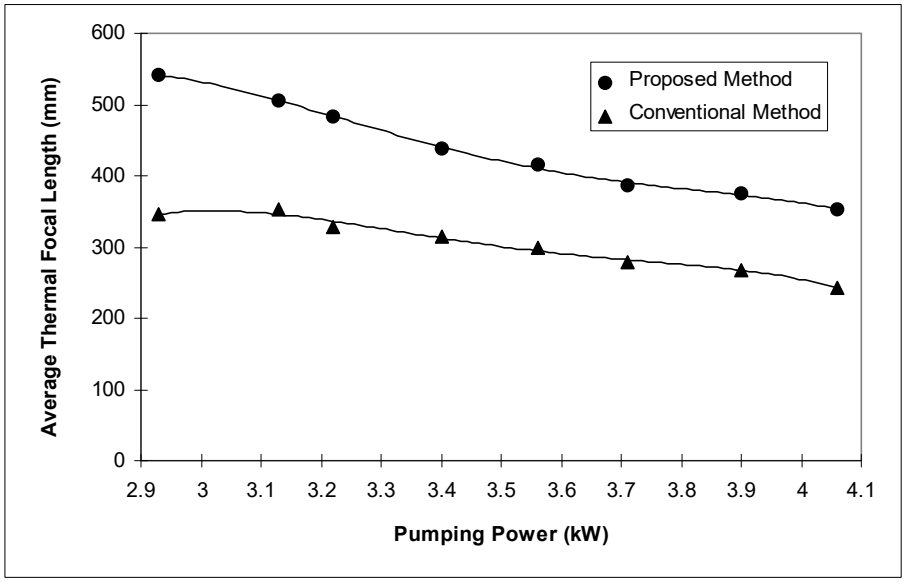

(a) Average thermal focal length

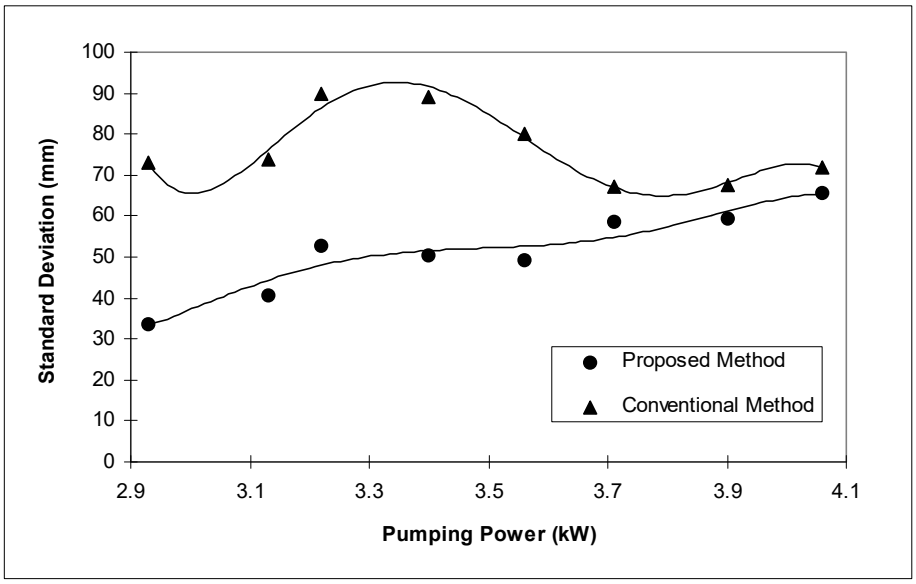

(b) Standard deviation of thermal focal length

Figure 4.9 Average thermal focal lengths & their standard deviations vs. pumping power

4.2.6 Related Observations

The energy distribution, M^2, and divergence angle of the HeNe laser beam corresponding to various pumping powers without any Nd:YAG laser resonator are shown in Figure 4.10. It is observed that the energy distributions are different at different pumping powers, which is caused by the thermally induced birefringence of the Nd:YAG rod. The thermal effect causes a significant decrease in output power and a marked change in beam shape [4.11].

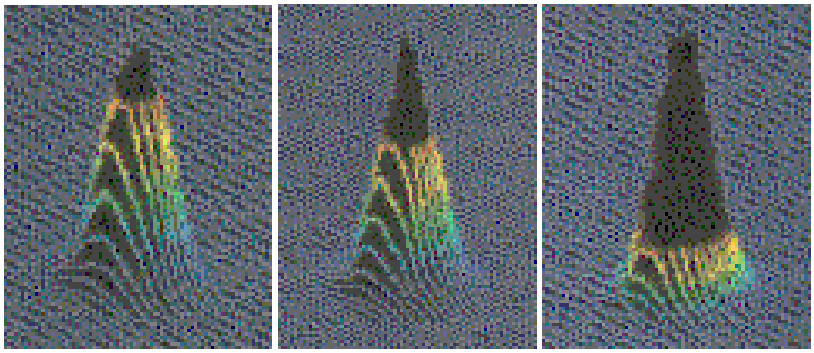

(a) No pumping (b) Pumping power: 1040 W (c) Pumping power: 2478 W

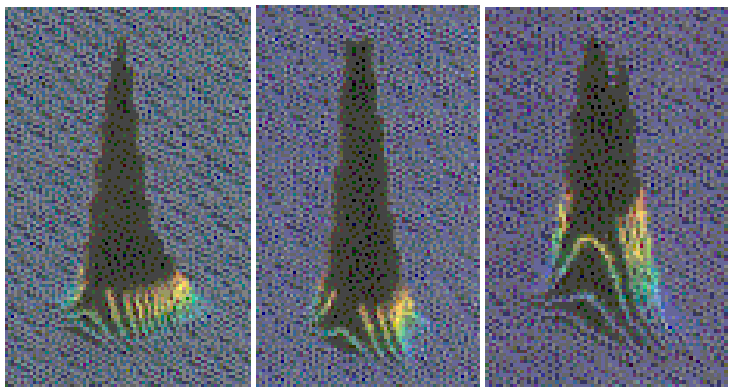

(d) Pumping power: 2928 W (e) Pumping power: 3556 W (f) Pumping power: 3900 W

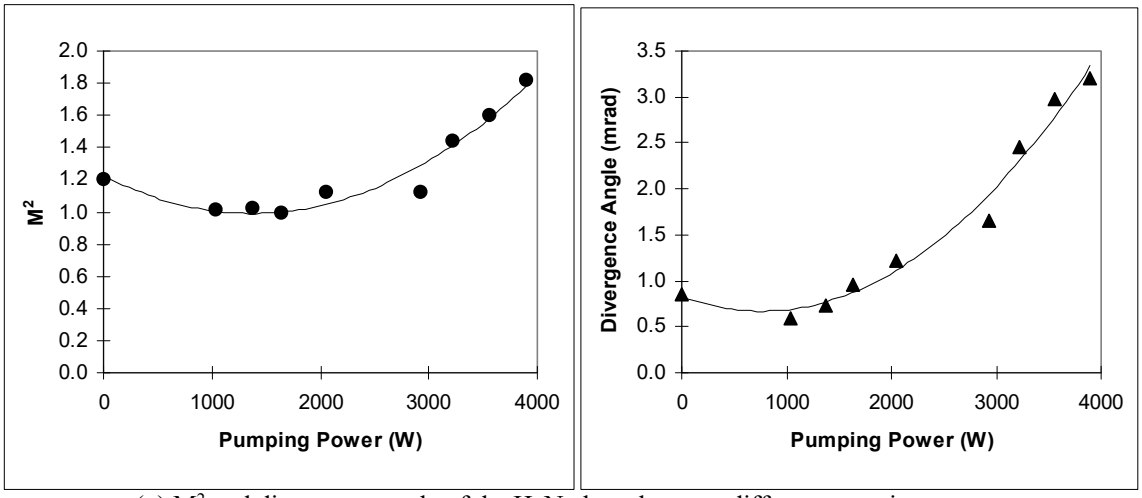

(g) M^2 and divergence angle of the HeNe laser beam at different pumping powers

Figure 4.10 Typical HeNe beam energy distribution, M^2,
and divergence angle at different pumping powers

When the Nd:YAG laser resonator was re-installed, the beam propagation factors for the YAG laser beam were measured at different pumping powers. The laser resonator consists of a rear mirror and an output coupler spaced at 670 mm, as shown in Figure 4.11. The rear mirror is plano-convex with a radius of curvature of 1 m and the output coupler is a plane mirror with a reflectivity of 85%. The results are given in Table 4.4, which shows that the beam quality of the YAG laser degraded with an increase in the pumping power.

Table 4.4 Variation of M^2 of a YAG laser beam at different pumping powers

Pumping power (kW)	3.08	3.22	3.40	3.56	3.90
Laser power (W)	45.5	46.9	47.9	53.1	56.9
M^2	4.96	5.32	5.86	6.36	6.91
Divergence (mrad)	8.12	8.58	9.43	10.15	10.19

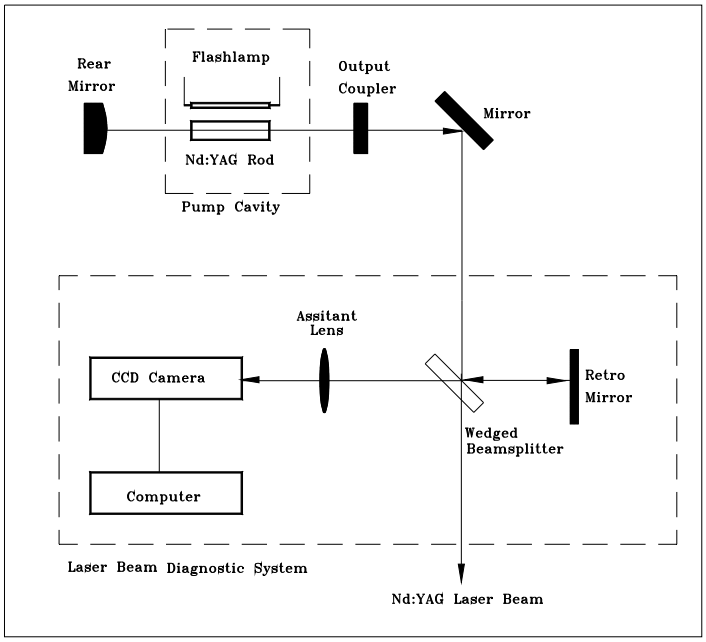

Figure 4.11 Experimental set-up for measuring
laser beam propagation factors of a Nd:YAG laser

The trends in the variation of the beam propagation factor M^2 with the pumping power for the HeNe and Nd:YAG laser beams are shown in Figure 4.12. It is observed that the trends are very similar. This means that the change in M^2 with the pumping power is mainly caused by thermal effects of the Nd:YAG rod, and that apart from a scaling factor, the propagation equations stated for the HeNe probe beam can be applied to the Nd:YAG laser beam.

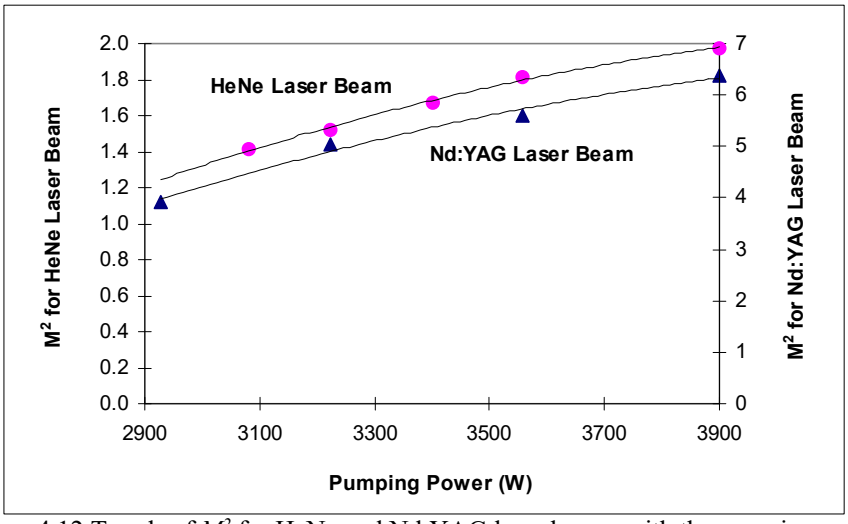

Figure 4.12 Trends of M^2 for HeNe and Nd:YAG laser beams with the pumping power

4.2.7 Section Summary

An exact formula to calculate the focal length of the thermal lens in solid-state lasers has been introduced. The procedures to use the formula are as follows:

(1) Measure the probe beam parameters with a beam diagnostic system: M^2, D_0 and Z_0.
(2) Measure the probe beam parameters after the beam has gone through the Nd:YAG rod that is being pumped but without resonator optics: Z_0', Z_1', Z_2 and D_0'.
(3) Calculate the focal lengths of the thermal lens and the percentage deviation using Equations (4.6), (4.7) and (4.9) - (4.11).
(4) Calculate the difference percentages using Equations (4.16) - (4.18).

Comparisons between the proposed method and the conventional method are summarised in Table 4.5.

Table 4.5 Comparisons between the proposed method and the conventional method

	Proposed method	Conventional method
Equipment required	Probe laser Laser beam diagnostic equipment	Probe laser Focusing lens
Beam energy distribution	Yes	No
Beam quality	Yes	No
Complexity	Relatively complex	Relatively simple
Accuracy	Good	Poor
Repeatability	Good	Fair

4.3 Investigation of Resonator Stability in the Presence of Thermal Lensing Effect

4.3.1 Laser Beam Propagation in Thermal Lensing Resonator

Figure 4.13 illustrates a resonator containing an internal thermal thin lens, often referred to as an active resonator. It consists of an output coupler M_1, a mirror M_2, and a thin lens (or an equivalent thermal lens for the Nd:YAG rod) [4.12]. The optics M_1 and M_2 have radii of curvature of R_1 and R_2, respectively. The parameters ω_{01} and ω_{02} are the beam waists on both sides of the thermal lens, which has a focal length of f_0, normally located at the centre of the laser rod.

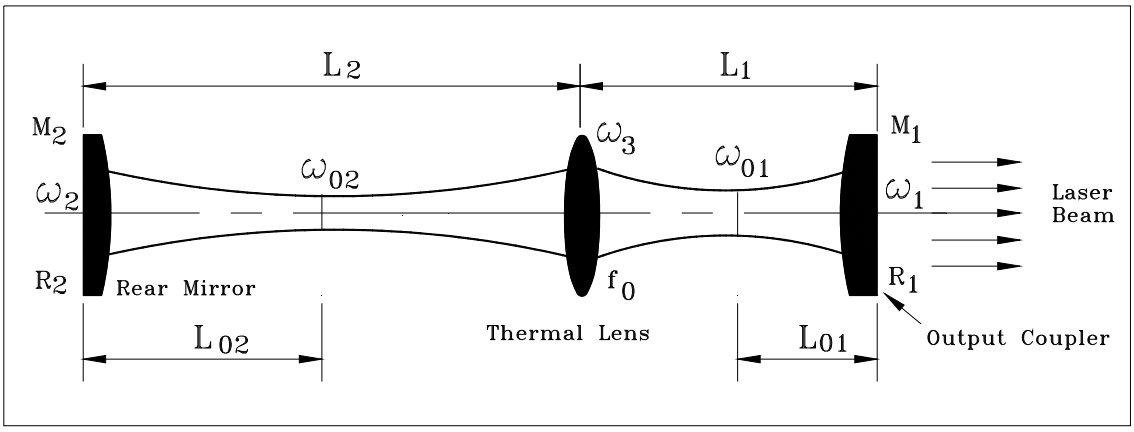

Figure 4.13 Active laser resonator with an internal thin lens

The pertinent parameters of an active resonator are [4.13]

$$G_1 = 1 - \frac{L_2}{f_0} - \frac{L_0}{R_1} \tag{4.23}$$

$$G_2 = 1 - \frac{L_1}{f_0} - \frac{L_0}{R_2} \tag{4.24}$$

$$G = G_1 G_2 \tag{4.25}$$

where $$L_0 = L_1 + L_2 - \frac{L_1 L_2}{f_0} \tag{4.26}$$

L_1 and L_2 are the spacings between the thermal lens and M_1 and M_2, respectively,
G_1, G_2, and G are defined as the "resonator G parameters", and
L_0 is called the effective resonator length.

The beam parameters in the resonator are given by

$$\omega_{01}^2 = \frac{\lambda L_0 \sqrt{G_1 G_2 \left(1 - G_1 G_2\right)}}{\pi \left[G_2 \left(L_0 / R_1 \right)^2 + G_1 \left(1 - G_1 G_2\right) \right]} \tag{4.27}$$

$$\omega_{02}^2 = \frac{\lambda L_0 \sqrt{G_1 G_2 (1 - G_1 G_2)}}{\pi \left[G_1 (L_0 / R_2)^2 + G_2 (1 - G_1 G_2) \right]} \tag{4.28}$$

$$L_{01} = \frac{L_0^2 G_2 / R_1}{G_2 (L_0 / R_1)^2 + G_1 (1 - G_1 G_2)} \tag{4.29}$$

$$L_{02} = \frac{L_0^2 G_1 / R_2}{G_1 (L_0 / R_2)^2 + G_2 (1 - G_1 G_2)} \tag{4.30}$$

The radii of the beam at M_1 and M_2 are

$$\omega_1^2 = \frac{\lambda L_0}{\pi} \sqrt{\frac{G_2}{G_1 (1 - G_1 G_2)}} \tag{4.31}$$

and

$$\omega_2^2 = \frac{\lambda L_0}{\pi} \sqrt{\frac{G_1}{G_2 (1 - G_1 G_2)}} \tag{4.32}$$

and the full divergence angle of the output laser beam in the far field, θ, is

$$\theta = \frac{2\lambda}{\pi \omega_{01}} \tag{4.33}$$

The far-field divergence (θ_m) of a higher order mode can be related to the corresponding parameters of the fundamental mode by [4.14]

$$\theta_m = \omega_1 \sqrt{m + 0.5} \tag{4.34}$$

where m is the transversal order of the mode in case of rectangular symmetry.

If a limiting aperture of radius of R' is placed inside the resonator, the number of oscillating modes is estimated by

$$m = \frac{R'^2}{\omega_{0a}^2} - 0.5 \tag{4.35}$$

where ω_{0a} is the radius of the TEM_{00} beam at the position of the aperture. If there is no aperture in the resonator, R' can be replaced by the rod radius R.

The multimode far-field divergence angle, θ, is given by

$$\left(\frac{L_0 \theta}{R} \right)^2 = \frac{4 \left[n_m^2 G_2 \left(L_0 / R_1 \right)^2 + G_1 (1 - G_1 G_2) \right] \bullet \left[G_2 \left(L_0 / R_1 \right)^2 + G_1 (1 - G_1 G_2) \right]}{G_1 G_2 (1 - G_1 G_2) + \left[\frac{L_1}{L_0} \left\{ G_2 \left(L_0 / R_1 \right)^2 + G_1 (1 - G_1 G_2) \right\} - G_2 \left(L_0 / R_1 \right) \right]^2} \tag{4.36}$$

where n_m is the refractive index of the substrate for the output coupler.

4.3.2 Stability Condition of Resonator with a Thermal Lens

The stability criterion of an active resonator is expressed by

$$0 < G_1 G_2 < 1 \tag{4.37}$$

Substituting Equations (4.23) and (4.24) into Equation (4.37), we get

$$0 < \left(1 - \frac{L_2}{f_0} - \frac{L_0}{R_1}\right)\left(1 - \frac{L_1}{f_0} - \frac{L_0}{R_2}\right) < 1 \tag{4.38}$$

From Equations (4.23) and (4.24), we obtain

$$G_1 = g_1 + \frac{L_2}{f_0}\left(\frac{L_1}{R_1} - 1\right) \tag{4.39}$$

$$G_2 = g_2 + \frac{L_1}{f_0}\left(\frac{L_2}{R_2} - 1\right) \tag{4.40}$$

$$G_2 - g_2 = \left(G_1 - g_1\right)\frac{\dfrac{L_1}{L_2} + g_2}{\dfrac{L_2}{L_1} + g_1} \tag{4.41}$$

where g_1 and g_2 are the g-parameters in a passive resonator (namely, $1/f_0 = 0$). Figure 4.14 shows that the point describing the resonator in the stability diagram moves along a straight line (Line a or Line b, related to the rod location in the resonator) from the point (g_1, g_2) as the dioptric power $1/f_0$ changes. The starting point (g_1, g_2) corresponds to the situation $f_0 = \infty$ or $D=0$ ($D = 1/f_0$, dioptric power). The lines pass through two stable and three unstable zones. The boundaries, in terms of dioptric power, are given by the following expressions [4.15]:

$$D_I = \frac{1}{L_1 - R_1} + \frac{1}{L_2 - R_2} \qquad (G_1G_2 = 1,\ G_1 > 0,\ G_2 > 0) \tag{4.42}$$

$$D_{II} = \frac{1}{L_2} + \frac{1}{L_1 - R_1} \qquad (G_1G_2 = 0,\ G_1 = 0) \tag{4.43}$$

$$D_{III} = \frac{1}{L_1} + \frac{1}{L_2 - R_2} \qquad (G_1G_2 = 0,\ G_2 = 0) \tag{4.44}$$

$$D_{IV} = \frac{1}{L_1} + \frac{1}{L_2} \qquad (G_1G_2 = 1,\ G_1 < 0,\ G_2 < 0) \tag{4.45}$$

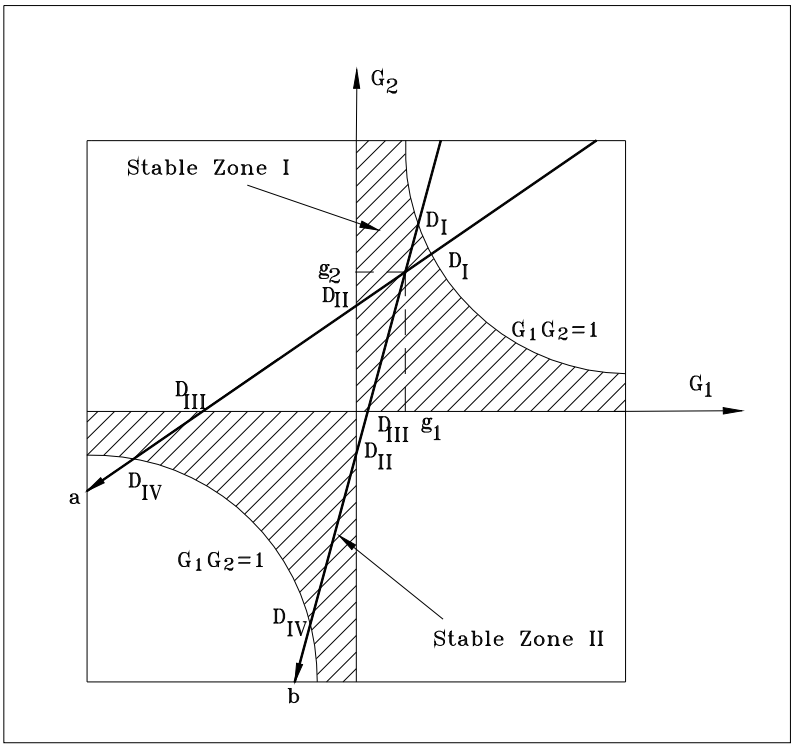

Figure 4.14 Stability diagram of a resonator with a thermal lens

The dioptric power can be expressed from Equations (2.5) and (2.6) as

$$D = \frac{C}{A} P_{in} \tag{4.46}$$

where C is a constant related to the thermal lensing conditions and the material properties, A is the rod cross-sectional area, and P_{in} is the pumping power.

The output laser power can be given by [4.16]

$$P_{out} = \eta_s \left(P_{in} - P_{th} \right) \tag{4.47}$$

where η_s is the slope efficiency and P_{th} the threshold pumping power.

Based on Equations (4.46) and (4.47), we obtain

$$\Delta D = \frac{C}{\eta_s A} \Delta P_{out} \tag{4.48}$$

This expression means that a wide output power range has a wide diopter range, which has a significant influence on the beam parameters. The resonator stability requires from Figure 4.14 that

$$\Delta D < \Delta D_C \tag{4.49}$$

where $\Delta D_C = D_{II} - D_I = D_{IV} - D_{III}$ when $D_{III} > D_{II}$ (4.50)

or $\Delta D_C = D_{IV} - D_{II} = D_{III} - D_I$ when $D_{III} < D_{II}$ (4.51)

Thus, $\Delta P_{out} < \Delta D_C \frac{\eta_s A}{C}$ (4.52)

When the pumping power makes the diopter change between the two neighbouring boundaries, the beam parameter product follows the expression [4.17]

$$\frac{2\lambda}{\pi} \le (\theta \bullet \omega) \le \Delta D_C \bullet R^2 \qquad (4.53)$$

where θ and ω are the full divergence angle and the beam radius, respectively, and R is the rod radius.

When the output laser power changes from *0* to $P_{out,max}$, the maximum beam parameter product is given from Equations (4.48) and (4.53) as [4.18]

$$\frac{(\theta \bullet \omega)_{\max}}{P_{out,\max}} = \frac{C}{\pi \eta_s} \qquad (4.54)$$

The above equation indicates that a beam parameter product will be large if the laser operates with a wide range of output laser power. It means that a small beam parameter product cannot be obtained if the output laser power varies widely.

As described in Equation (4.36), the relationship between the dioptric power D of the rod, the resonator parameters R_1, R_2, L_1, L_2, and the resulting multimode divergence θ is very complex. The G-parameters and the effective length L_0 all depend on D values. To understand the behaviour of such a system, the following discussions are focused on some special resonators.

4.3.3 Stability of a Plane-Parallel Resonator with an Internal Thin Lens

The stability diagram of a plane-parallel resonator, i.e. $R_1 = R_2 = \infty$, is shown in the $\left(L_1/f_0, L_2/f_0\right)$ plane in Figure 4.15. The equations applied are

$$G_1 = 1 - \frac{L_2}{f_0} \quad \text{and} \quad G_2 = 1 - \frac{L_1}{f_0} \qquad (4.55)$$

Equation (4.36) can be rewritten as [4.2]

$$\theta = \frac{2R}{L}\sqrt{\frac{DL(1-DL_2)}{1-2DL_2\left(1-\frac{L_2}{L}\right)}} \qquad (4.56)$$

where L = L_1 + L_2 and R is the rod radius. Figure 4.16 shows the computed divergence angle as a function of dioptric power D for a plane-parallel resonator using Equation (4.48). Here $R = 4$ mm. The upper limit of the divergence angle and the minimum diffraction-limited divergence angle are 26.7 mrad $\left(= R/L_{01}\right)$ and 0.2 mrad $\left(= 2\lambda/\pi R\right)$, respectively [4.14]. It is interesting to note that with an increase in D values, the beam divergence starts to increase from zero to a maximum, and then decreases. Further increment in dioptric power makes the resonator unstable.

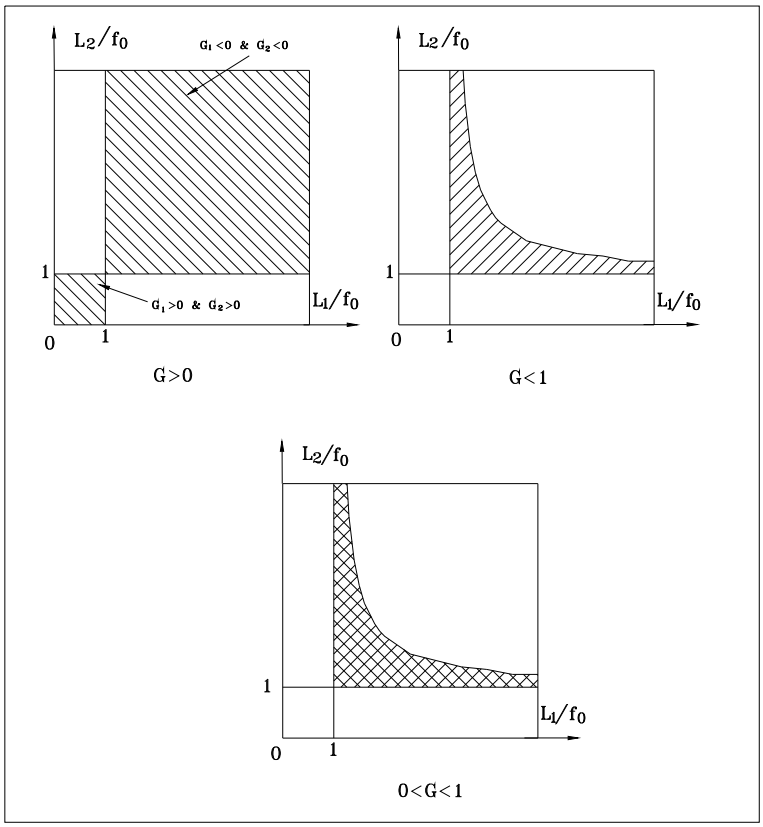

Figure 4.15 Stability diagram of plane-parallel resonator

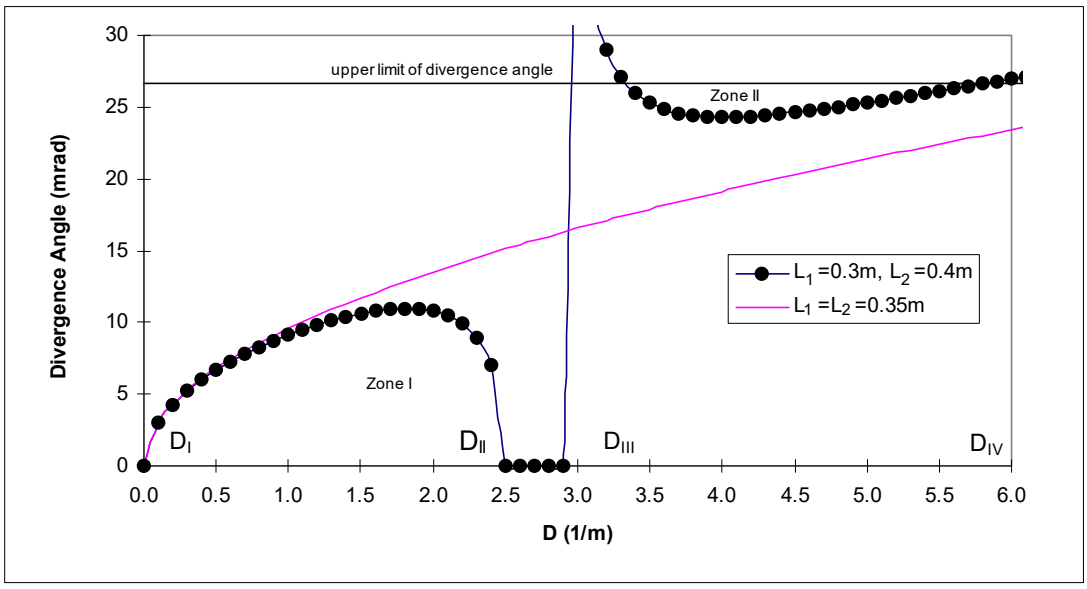

Figure 4.16 Divergence angle vs. dioptric power D for a plane-plane resonator
(Here $D_I = 0$, $D_{II} = 2.5\ m^{-1}$, $D_{III} = 3.3\ m^{-1}$ & $D_{IV} = 5.8\ m^{-1}$)

4.3.4 Stability of a Resonator with an Internal Thin Lens Close to a Flat Output Coupler

For a resonator with a flat output coupler, M_1, next to a thin lens or a thermal lens (i.e., L_1 can be considered as 0 compared to L_2 and $L = L_1 + L_2 \approx L_2$), as shown in Figure 4.17. The stability diagram of this resonator is shown in Figure 4.18. The shaded regions are shown for the conditions of (a) $G < 0$ and (b) $G < 1$. The overlap region, in solid black, corresponds to the stability zone $0 < G < 1$. The equations used are

$$G_1 = 1 - \frac{L}{f_0} \qquad \text{and} \qquad G_2 = 1 - \frac{L}{R_2} \qquad (4.57)$$

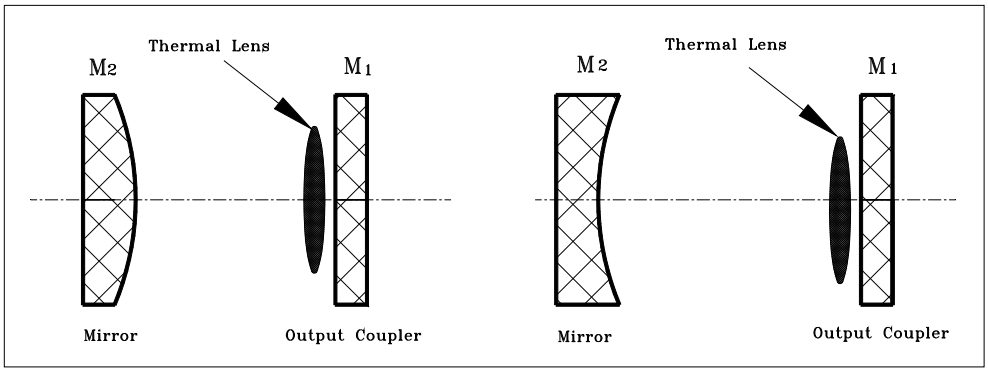

Figure 4.17 A resonator with $L_1 = 0$ and $R_1 = \infty$

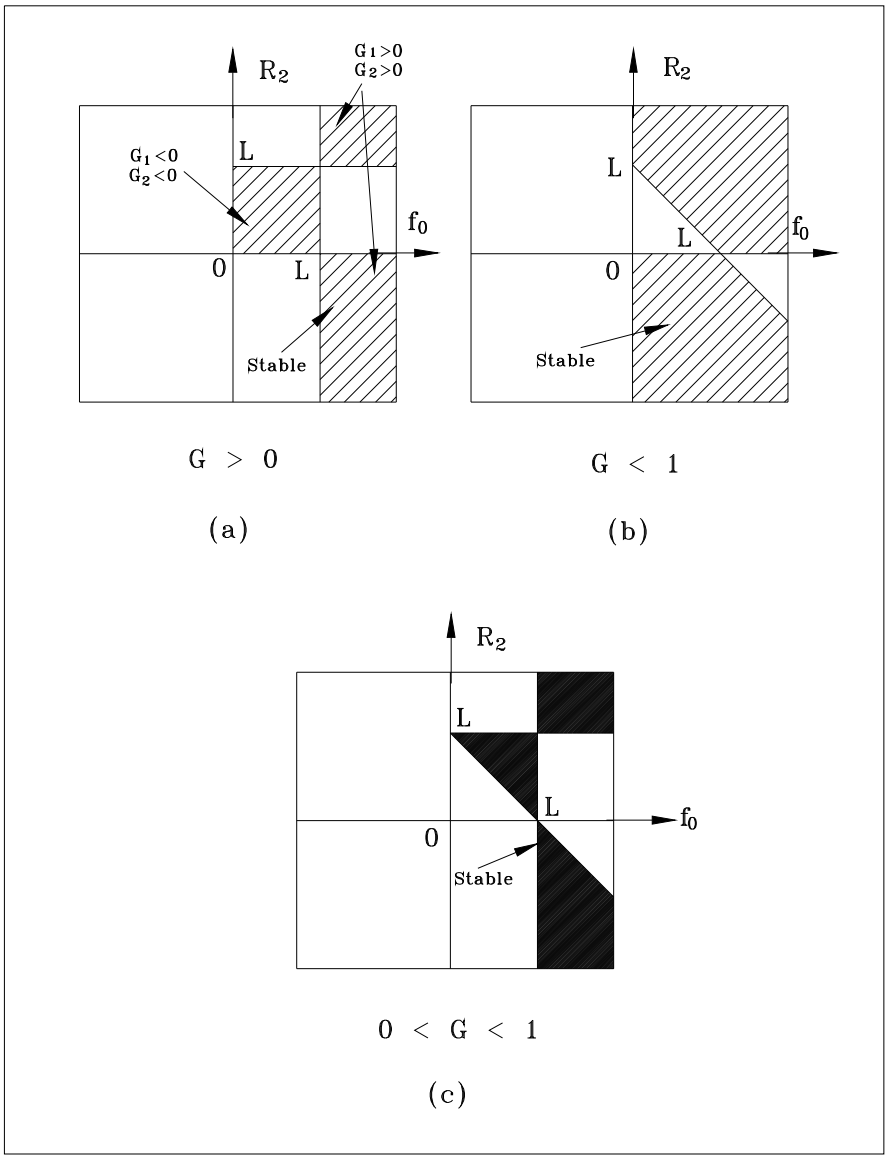

Figure 4.18 Stability diagram of a resonator with $L_1 = 0$ and $R_1 = \infty$

Since a laser may work over a wide range of pumping powers, the thermal lensing effect will vary according to different pumping powers. Therefore the stability of the output beam is sensitive to the thermal focal length. Figure 4.19 illustrates the relationship between gaussian beam divergence angle and the thermal focal length of some typical resonators using Equation (4.33). The resonator parameters at $L = 0.7$ m and $R_2 = 0.5$ m show the least variation in the divergence angle when the thermal focal length changes from 0.3 m to 0.5 m. The relevant divergence angle fluctuation is only ±3.8 %. The variations in the divergence angle for the other resonators are larger. Thus they are not feasible for practical applications.

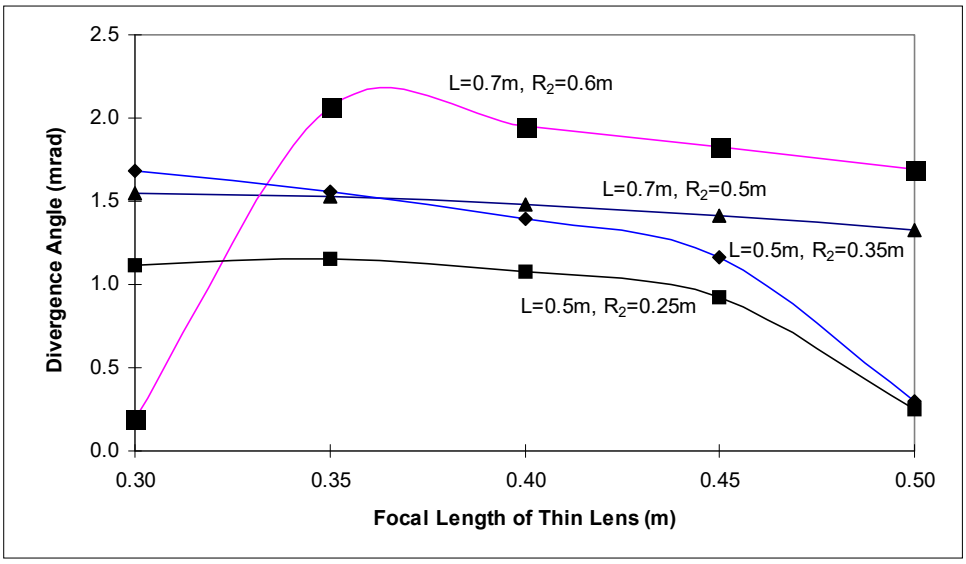

Figure 4.19 Divergence angle vs. focal length
of thin lens for the resonators with $L_1 = 0$ and $R_1 = \infty$

4.3.5 Stability of Different Types of Active Resonators

In general, the analysis is similar to those presented in sections 4.3.3 and 4.3.4. In this section, some examples of plane-convex, convex-convex and concave-convex resonators are considered. The divergence angles computed with Equation (4.33) are shown in Figure 4.20, where $L = 0.7$ m. For the resonator with $R_1 = R_2 = -0.8$ m and $L_1 = 0.3$ m, the divergence angles change from 3.68 mrad to 3.72 mrad when the thermal focal lengths change from 0.3 m to 0.5 m, respectively. The relative variations in the divergence angles fall only within ±0.27%. The discontinuities in the other two curves indicate resonator instability. From Figure 4.20, it is obvious that the resonator configuration with $R_1 = -0.8$ m and $R_2 = -0.8$ m is the best. In fact, this is the configuration adopted by the NEC laser.

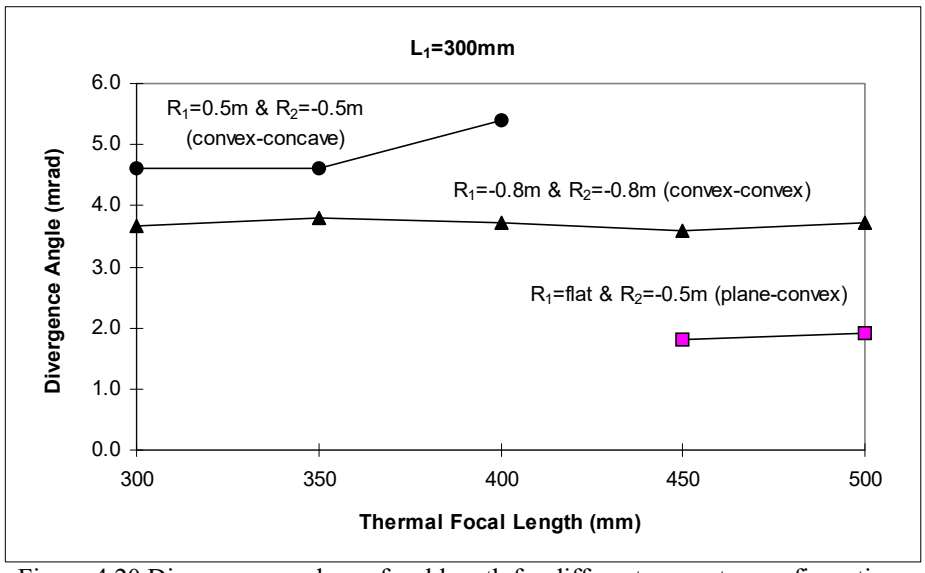

Figure 4.20 Divergence angle vs. focal length for different resonator configurations

4.3.6 Influence of Laser Rod Position on Resonator Stability

It has been shown in the previous section that the (G_1, G_2) plane illustrates the behaviour of the stable resonators with an internal thermal lens. For a quantitative description, this figure must be complemented by a second stability diagram showing the stability limits given by Equations (4.42) - (4.45). The stability limit is a function of the rod position (L_1) inside the resonator for a given resonator length. As an example, Figure 4.21 shows the stability limits for the resonator consisting of $R_1 = \infty$, $R_2 = -100$ cm, and $L_1 + L_2 = 70$ cm. Therefore, if L_1 is set at 38 cm, stability can be achieved through a thermal lens of 0.0075 cm^{-1} to 0.031 cm^{-1} and 0.034 cm^{-1} to 0.057 cm^{-1}, i.e. 175 mm to 294 mm and 323 mm to 1333 mm.

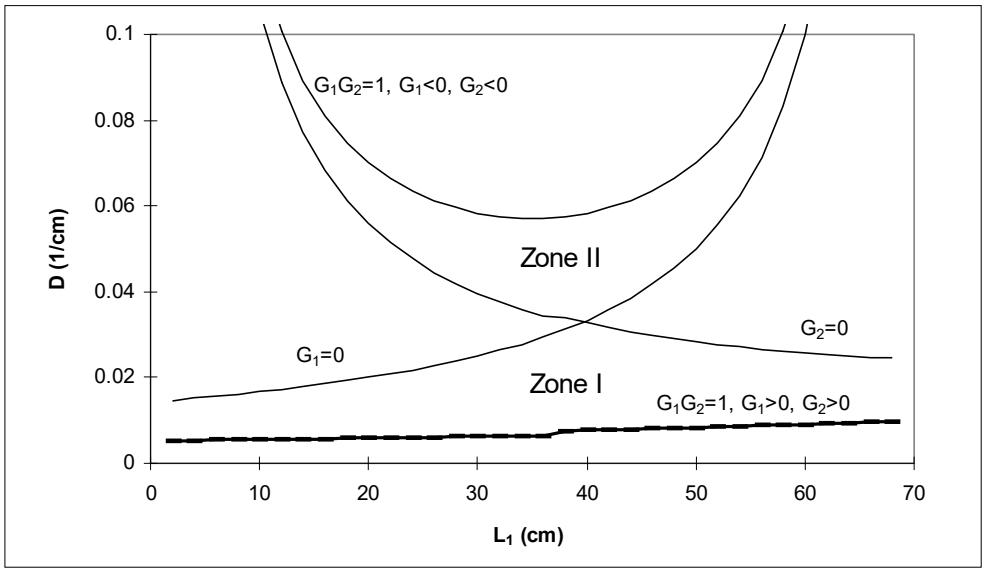

Figure 4.21 Boundaries of the two stability zones as a function of the rod position L_1

4.3.7 Thermally Insensitive Resonator with Respect to Laser Rod Position

In this section, we present a systematic method to search for a thermally sensitive resonator with respect to laser rod position. Previous analyses show that there are always two stability zones associated with the same width in terms of dioptric power, as the thermal focal length varies. The pump-induced fluctuations in the focal length may strongly perturb the laser performance, even preventing any practical or reliable use of the laser. It is therefore necessary to design a resonator insensitive to the diopter change for practical uses of the laser.

Referring to Figure 4.13, we start with Equation (4.31) [or Equation (4.32)] to find the spot size ω_3 on the lens. For Gaussian beam propagation, the following equations apply [4.19]

$$\omega_3^2 = \frac{\lambda}{\pi}\sqrt{\frac{4u_1u_2G_1G_2 + (u_1-u_2)^2}{(1-G_1G_2)G_1G_2}} \tag{4.58}$$

or

$$\omega_3^2 = \frac{\lambda}{\pi}\frac{|2xu_1u_2 + u_1 + u_2|}{\sqrt{(1-G_1G_2)G_1G_2}} \tag{4.59}$$

where three new variables u_1, u_2 and x are introduced to simplify the following analysis:

$$u_1 = L_1\left(1-\frac{L_1}{R_1}\right), \qquad u_2 = L_2\left(1-\frac{L_2}{R_2}\right) \tag{4.60}$$

$$G_1 = -\frac{L_2}{L_1}(1+xu_1), \qquad G_2 = -\frac{L_1}{L_2}(1+xu_2) \tag{4.61}$$

and $$x = \frac{1}{f_0} - \frac{1}{L_1} - \frac{1}{L_2} \tag{4.62}$$

Equation (4.58) shows that ω_3 goes to infinity for both $G_1G_2 = 0$ and $G_1G_2 = 1$. This infers that there always exists a point within the stability zone at which ω_3 is minimum. Furthermore, reliable mode operation requires the spot size, ω_3, in the rod to be stationary with respect to the thermal focal length, i.e. [4.20]

$$\frac{d\omega_3}{dD} = \frac{d\omega_3}{dx} = 0 \tag{4.63}$$

If this condition is satisfied, the resonator is said to be a dynamically stable resonator.

By solving the equation for product G_1G_2, we obtain [4.19]

$$G_1G_2 = (G_1G_2)_{sta} = \frac{1}{2}\left(1 - \frac{u_2}{u_1}\right), \qquad |u_1| > |u_2| \tag{4.64}$$

or

$$G_1G_2 = (G_1G_2)_{sta} = \frac{1}{2}\left(1 - \frac{u_1}{u_2}\right), \qquad |u_1| < |u_2| \tag{4.65}$$

Therefore, by inserting Equation (4.65) into Equation (4.58), the stationary value of the spot size on the lens, ω_{30}, is given by

$$\omega_{30}^2 = \frac{2\lambda}{\pi} max\left(|u_1|, |u_2|\right) \tag{4.66}$$

It is noted that the left-hand side of Equation (4.64) is a function of f_0 and L_1, but the right-hand side is only a function of L_1. If we assume that

$$p = \frac{1}{2}\left(1 - \frac{u_2}{u_1}\right), |u_1| > |u_2| \tag{4.67}$$

where p is a variable, and substituting Equations (4.62) and (4.67) into Equation (4.64), we obtain [4.21]

$$\left(\frac{1}{f_0}\right)_{sta,\pm} = \frac{-(u_1+u_2) \pm \sqrt{(u_1+u_2)^2 - 4u_1u_2(1-p)}}{2u_1u_2} + \frac{1}{L_1} + \frac{1}{L-L_1} \tag{4.68}$$

where $\left(\frac{1}{f_0}\right)_{sta}$ is the thermal focal length for which the spot size in the rod is stationary, and the ± sign indicates that there are two stationary points for each value of thermal focal length corresponding to Zone I and Zone II in Figure 4.14.

Case A: For a given resonator, namely R_1, R_2, and $L = L_1 + L_2$ are known, the influence of rod position on a thermal insensitive resonator is described by Equations (4.61), (4.64), (4.67), and (4.68). A typical diagram is shown in Figure 4.22, where $R_1 = -120$ cm, $R_2 = 100$ cm, and $L = 137$ cm. It can be observed from the figure that:

(1) there is a stable zone for each rod position for a given range of pumping power (or of thermal lensing focal length). The zone corresponding to $|u_1| < |u_2|$ (namely $L_1 < 20$ cm) is Zone II, and that corresponding to $|u_1| > |u_2|$ is Zone I;
(2) the focal length of the thermal lens corresponding to a dynamically stable resonator varies with rod position from Equation (4.68);
(3) the G_1G_2 parameter of a dynamically stable resonator will change with rod position. The rates of change at different zones are, however, different [4.19]. The rate in Zone I is smaller than that in Zone II. Therefore, it is better to operate the laser in Zone I by choosing a proper value of L_1.

Case B: In a practical application, the rod diameter is selected according to the laser power required. In this case, ω_{30} of the spot size in the rod and $\left(\frac{1}{f_0}\right)_{sta}$ are known parameters. It may be further assumed that $|u_1| > |u_2|$, which is not a restrictive condition since the resonator configurations for which $|u_1| < |u_2|$ can be immediately reduced to Case A by simply changing the positions of the cavity reflectors. The problem is how to search for a thermally sensitive resonator.

Using the above formulas, the following equations are obtained [4.17]

$$u_1 = \pm\frac{\pi}{2\lambda}\omega_{30}^2 \qquad \text{and} \qquad u_2 = -u_1\frac{2x_0u_1+1}{2x_0^2u_1^2+2x_0u_1+1} \tag{4.69}$$

and

$$\frac{1}{R_1} = \frac{1}{L_1}\left(1-\frac{u_1}{L_1}\right) \qquad \text{and} \qquad \frac{1}{R_2} = \frac{1}{L_2}\left(1-\frac{u_2}{L_2}\right) \tag{4.70}$$

where x_0 is the value of x calculated for $f = f_0$.

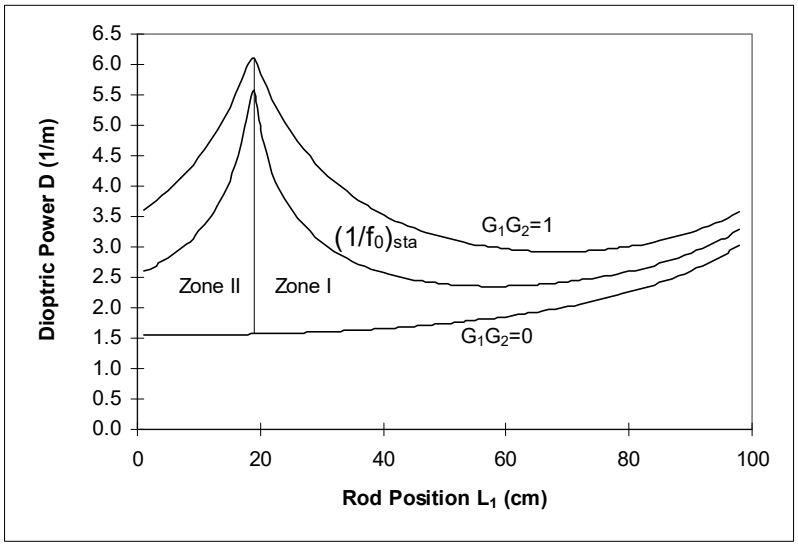

(a) Boundaries of stable zones and working points
insensitive to thermal lensing effects as a function of L_1

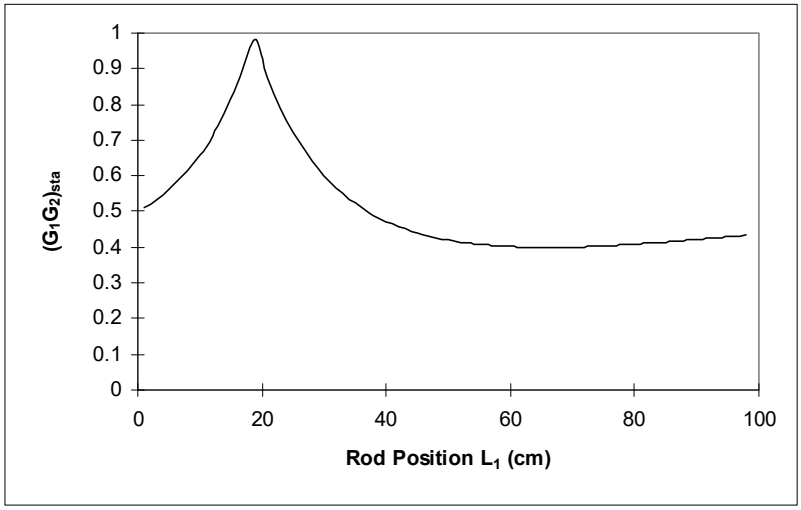

(b) G vs. L_1 when the spot size in the rod is stationary

Figure 4.22 Influence of rod position on a thermally insensitive resonator

Figure 4.23 provides the plots of the above equations for a few values of f_0 and ω_{30} in the case of the Nd:YAG laser wavelength of 1.064 μm. The parameters used are: $L = 137$ cm, $f_0 = 50$ or 35 cm, $\omega_{30} = 2$ mm.

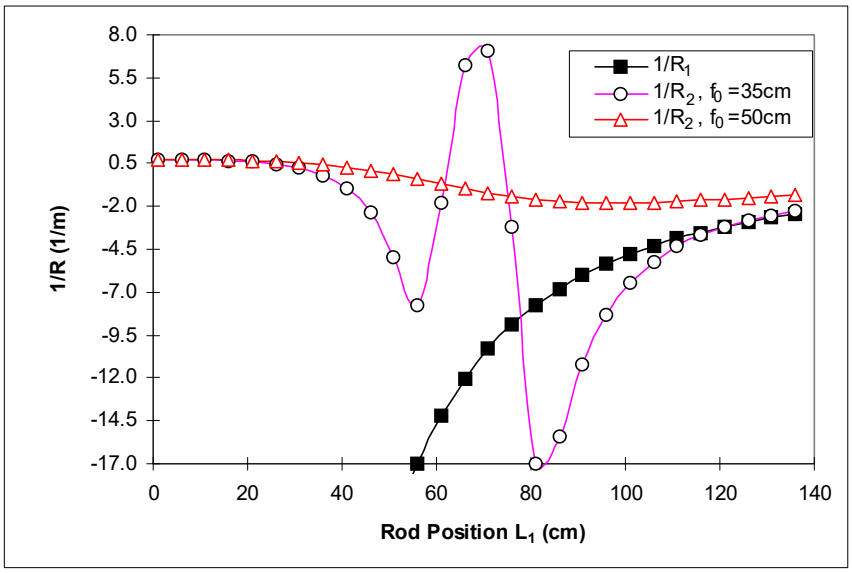

(a) $u_1 > 0$

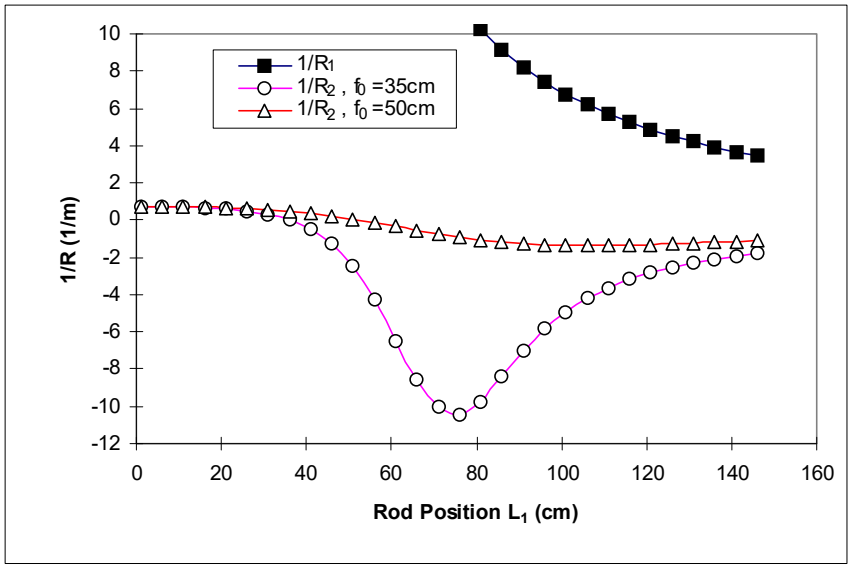

(b) $u_1 < 0$

Figure 4.23 Mirror curvatures $1/R_1$ and $1/R_2$ vs. L_1
for determination of the optimised resonator configuration

Now let us give an example of the use of Figure 4.23. If we wish to design a resonator for a spot radius of 2 mm on a rod with $f_0 = 50$ cm, we assume that $L = 137$ cm and $u_1 > 0$. From Figure 4.23(a), we read $1/R_1 = -7.76$ m^{-1} (or $R_1 = -129$ mm) and $1/R_2 = -1.59$ m^{-1} (or $R_2 = -629$ mm) if L_1 is selected to be 101 cm and $1/R_1 = -4.8$ m^{-1} (or $R_1 = -208$ mm) and $1/R_2 = -1.79$ m^{-1} (or $R_2 = -559$ mm) if L_1 is selected to be 101 cm. After determining the resonator configuration based on Figure 4.23, one must also check that small variation in the parameters such as R_1 and R_2, for example, due to construction tolerances or to errors in positioning the rod, does not strongly affect the mode volume or position of the stability zone along the $1/f_0$ axis.

4.3.8 Case Study

In Sections 4.2, we illustrate how to calculate the thermal focal length of an actively-pumped laser rod. In this section, we look at the stability regime of a typical laser cavity.

The experiments were performed using the NEC Nd:YAG laser. The parameters used were: $R_1 = \infty$, $R_2 = -1000$ mm, $L_1 = 310$ mm, $L_2 = 360$ mm, $R = 2$ mm. The thermal focal lengths are read from Figure 4.9(a) and are reproduced in Figure 4.24 again for ready reference. After the beam diameter and the divergence angle are measured, the beam parameter product is calculated using Equation (2.8) and shown as a function of pumping power in Figure 4.25. It is observed from Figure 4.24 and Figure 4.25 that the thermal focal length decreases and the beam parameter product increases with an increase in pumping power. It means that the thermal lensing effects do degrade the laser beam

quality. Based on Equation (4.53) the beam parameter product is calculated to be 0.68 to 8.2 mm.mrad, which agrees with the experimental results of 3.33 to 4.69 mm.mrad.

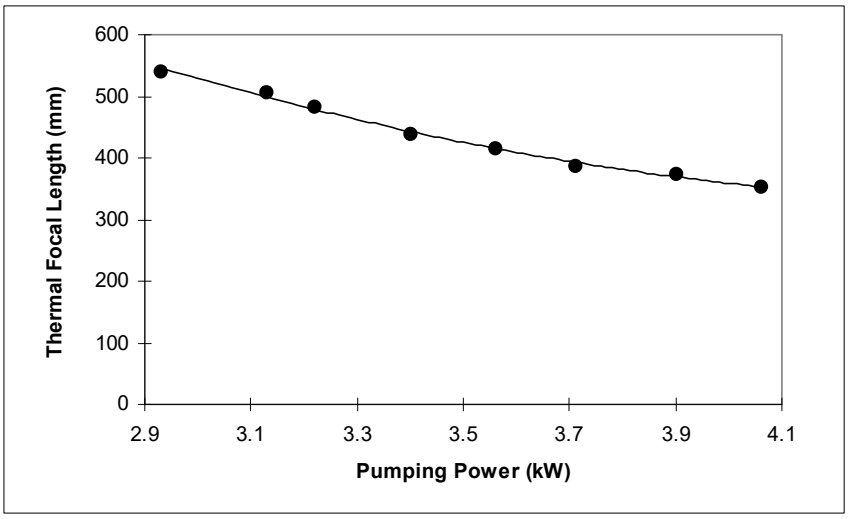

Figure 4.24 Thermal focal length vs. pumping power

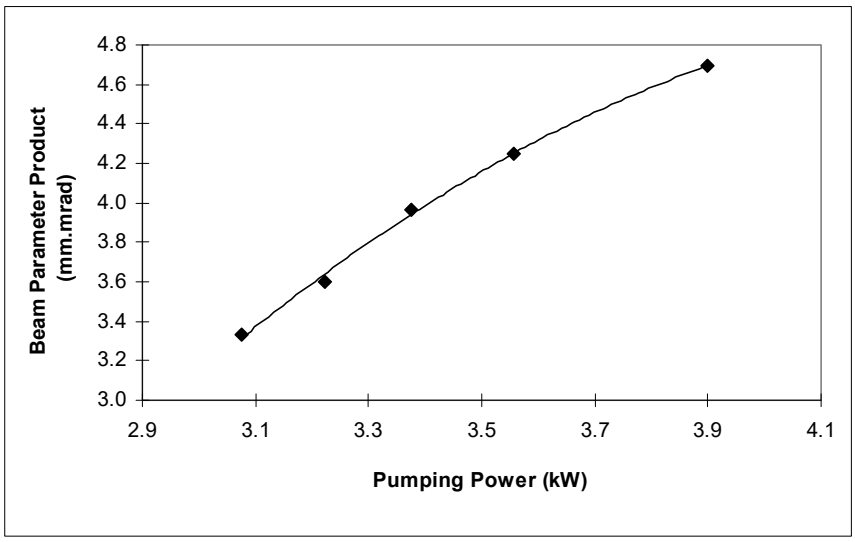

Figure 4.25 Beam parameter product vs. pumping power

Substituting the following resonator parameters that are used in the experiment into Equation (4.41):

$$\left.\begin{aligned} R_1 &= \infty \\ R_2 &= -1000\ mm \\ L_1 &= 310\ mm \\ L_2 &= 360\ mm \\ R &= 2\ mm \end{aligned}\right\} \qquad (4.71)$$

we obtain

$$G_2 = 1.17G_1 + 0.5 \qquad (4.72)$$

The stability diagram is shown in Figure 4.26. The boundaries in terms of dioptric power, according to Equations (4.42) - (4.45), are 0.74, 2.8, 3.86, and 6 m^{-1}, respectively. Figure 4.26 shows that the resonator without thermal lensing, i.e. (g_1, g_2), is unstable. The resonator moves along the line from (g_1, g_2) with increasing dioptric power. The resonator is stable with the focal length ranging from 1.35 m (D_I) to 0.357 m (D_{II}), or from 0.257 m (D_{III}) to 0.167 m (D_{VI}). It is shown that the focal lengths of the thermal lens calculated with the new equations lie in Zone I, and those calculated with the conventional equations lie partially in the unstable zones.

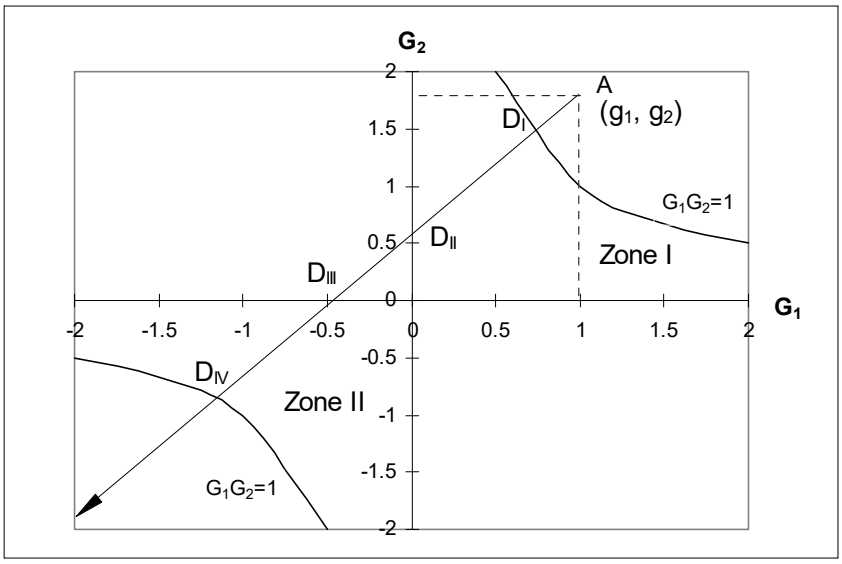

Figure 4.26 Stability diagram of the experimental resonator

Substituting Equation (4.71) into Equations (4.60) - (4.62), we get

$$\left.\begin{array}{ll} G_1 = 1 - 359.6D & G_2 = 1.67 - 421D \\ u_1 = 310\ mm & u_2 = 489.6\ mm \end{array}\right\} \qquad (4.73)$$

Substituting Equation (4.73) into Equation (4.59), we get

$$\omega_3^2 = 0.34 \times 10^{-4} \times \frac{302783.2D - 1017.1}{\sqrt{(1.67 - 780.6D + 151391.D^2) \times (-0.67 + 780.6D - 151391.6D^2)}} \qquad (4.74)$$

Figure 4.27 shows the beam radius on the thermal lens as a function of dioptric power using Equation (4.74). It is observed that the change in the beam radius is small when the thermal lensing focal length (or dioptric power) varies near the centres of the stable zones.

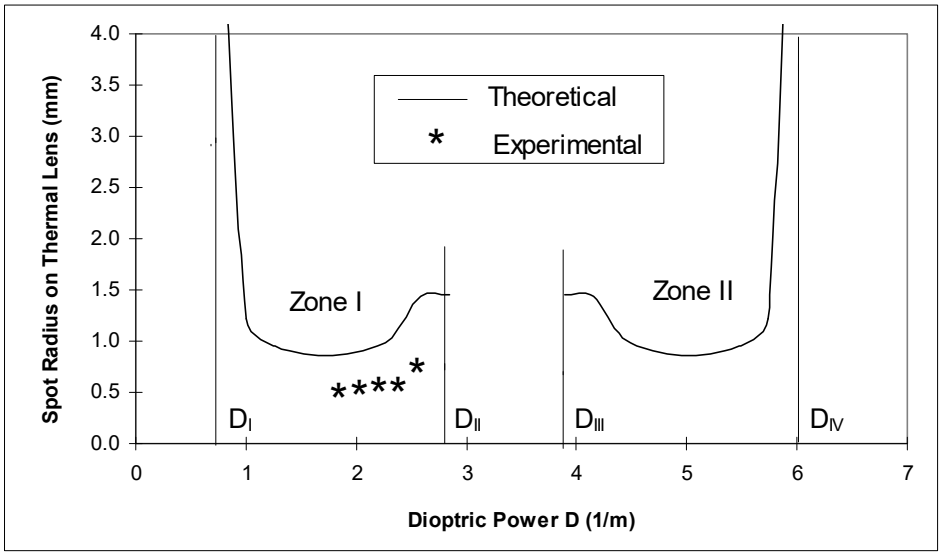

Figure 4.27 Beam radius on the thermal lens vs. dioptric power
Here, $D_I = 0.74\ m^{-1}$, $D_{II} = 2.8\ m^{-1}$, $D_{III} = 3.86\ m^{-1}$ and $D_{IV} = 6\ m^{-1}$.

Within the operating region of the NEC laser for input powers of 2.9 kW to 4.1 kW, it can be observed that the spot radius of the Gaussian beam falls within the size of the laser rod, and into the stable region of the cavity design.

4.4 Investigation of Laser Beam Quality

4.4.1 Investigation of Fundamental Nd:YAG Laser Beam Quality

The experiments on laser beam quality were performed on the NEC Nd:YAG laser.

4.4.1.1 M^2 at Various Pumping Powers

The equivalent resonator diagram is shown in Figure 4.28. The measured thermal focal length is 415 mm at the pumping power of 3556 W (please refer to Figure 4.9 or Figure 4.24). Based on laser resonator theory [4.13], the *G* parameter is 0.65, which means that the equivalent resonator is stable. The beam waist, spot size at rear mirror, spot size at the output coupler are 0.74 mm, 1.02 mm, and 0.94 mm in diameter, respectively. The beam waist is outside the rear mirror at 390 mm. The beam far-field divergence is 1.83 mrad in full angle. The theoretical value of M^2 should be 1.0 for a TEM_{00} mode by definition.

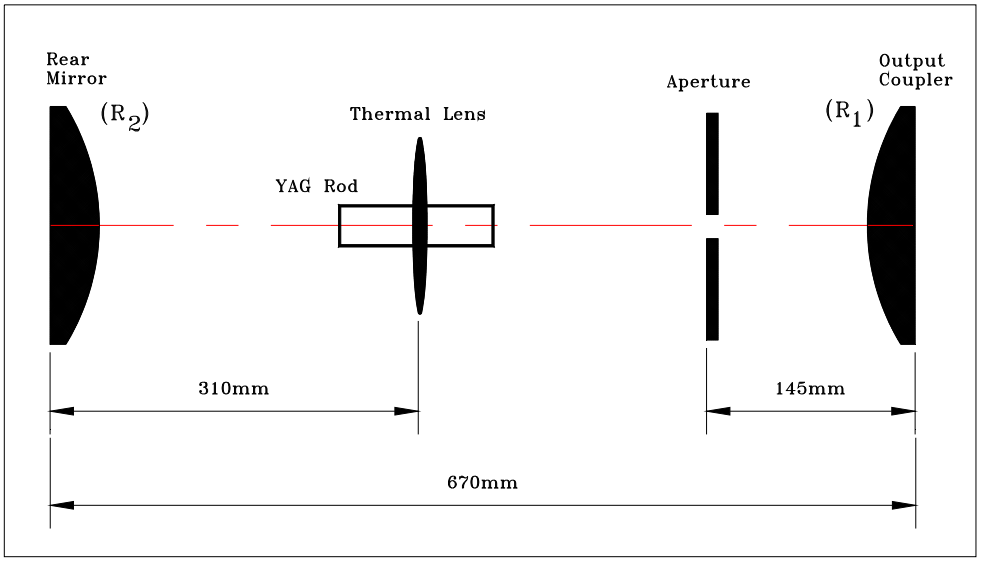

Figure 4.28 Equivalent resonator diagram

Figure 4.29 shows the measured beam propagation factors at different pumping powers. The results show that the beam propagation factors are all higher than 1, which means that the laser operates at multi-modes. The beam quality becomes worse and divergence becomes larger with an increase in the pumping power. This is due to a temperature- and stress-dependent variation of the index of refraction [4.13]. The temperature gradients generate mechanical stresses in the laser rod. The thermally induced birefringence causes a significant decrease in output power and a marked change in beam shape.

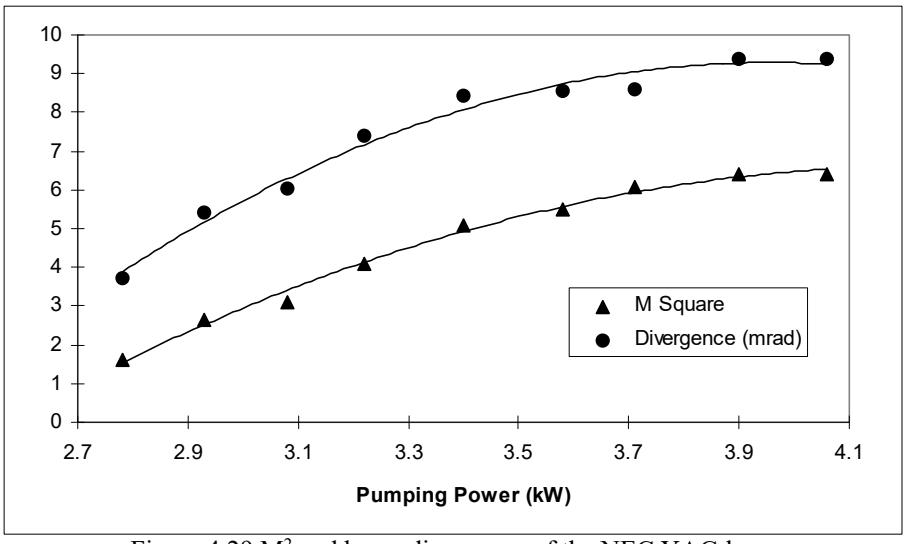

Figure 4.29 M^2 and beam divergence of the NEC YAG laser at different pumping powers

Figure 4.30 shows the 3D distributions of the laser beam energy at different pumping powers. It is evident from Figure 4.30(a-h) that the oscillation mode orders are higher at higher pumping powers.

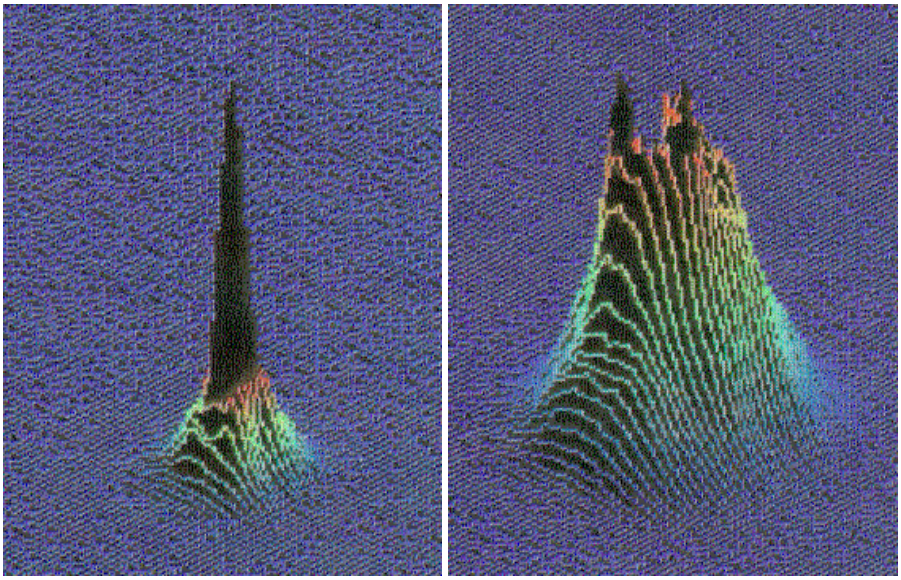

(a) Pumping power: 2.27 kW (b) Pumping power: 2.42 kW

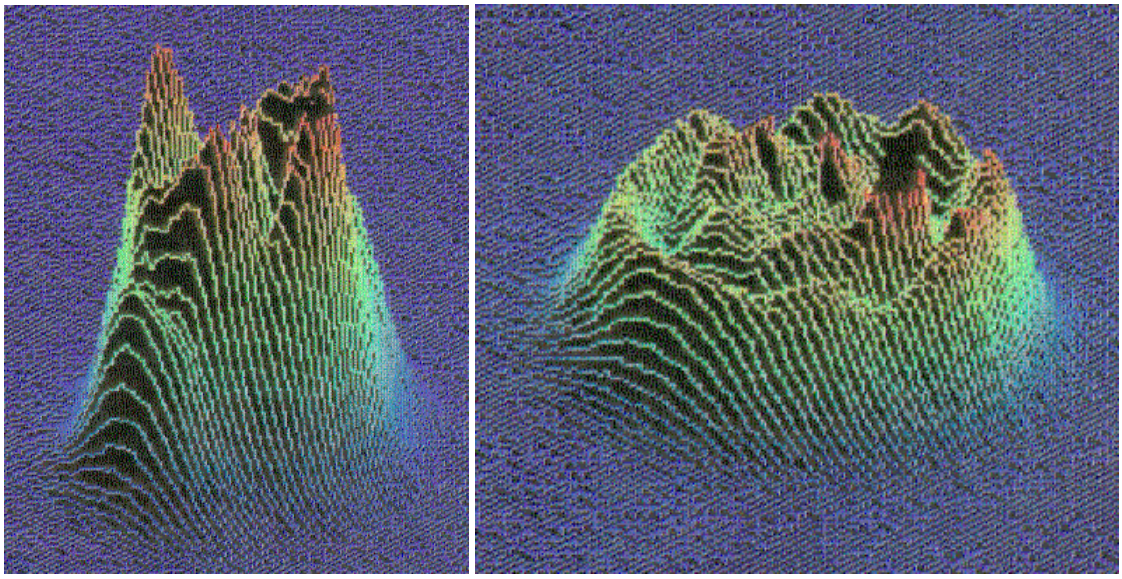

(c) Pumping power: 2.74 kW (d) Pumping power: 3.08 kW

Figure 4.30 3D distributions of laser beam energy at different pumping powers
(to be continued)

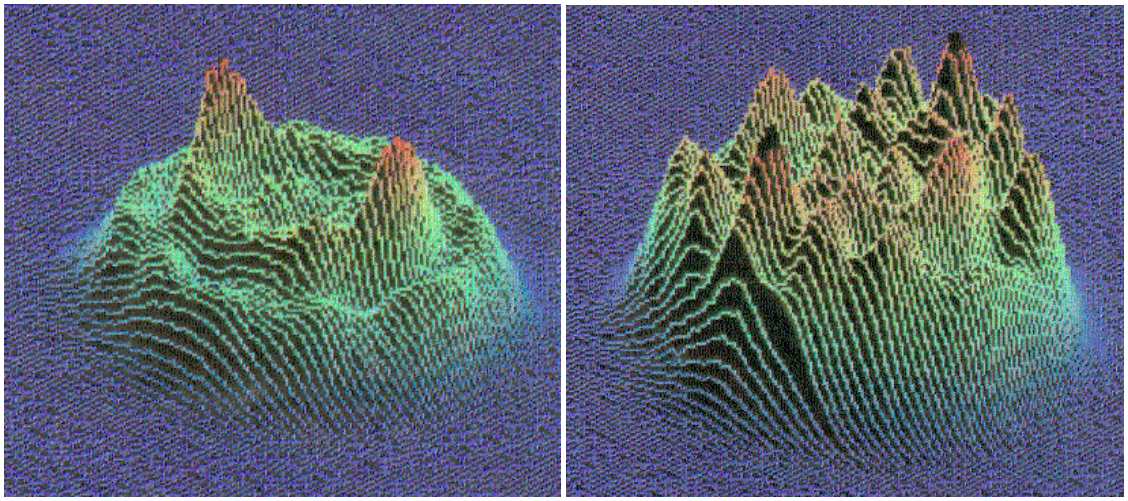

(e) Pumping power: 3.22 kW (f) Pumping power: 3.38 kW

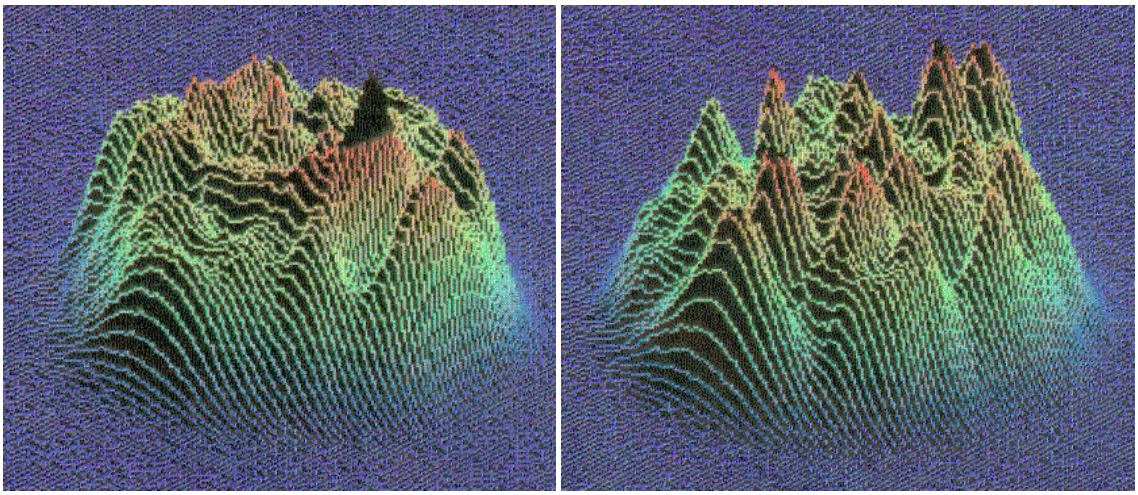

(g) Pumping power: 3.56 kW (h) Pumping power: 3.90 kW

Figure 4.30 3D distributions of laser beam energy at different pumping powers

Figure 4.31 shows the cross-sectional energy distributions at different pumping powers, corresponding to those shown in Figure 4.30. It is observed from Figure 4.31(a) that the energy distribution at the pumping power of 2.27 kW resembles a TEM_{00} mode but the other energy distributions contain multi-modes.

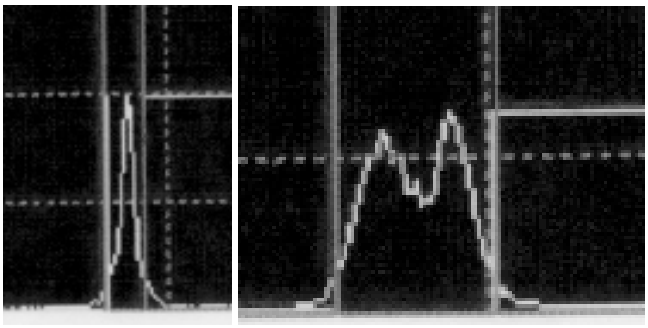

a) Pumping power: 2.27 kW (b) Pumping power: 2.42 kW

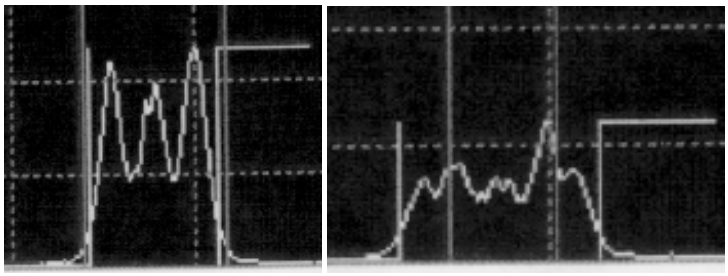

(c) Pumping power: 2.74 kW (d) Pumping power: 3.08 kW

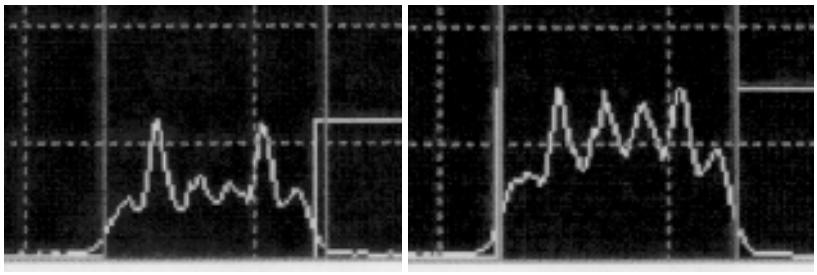

(e) Pumping power: 3.22 kW (f) Pumping power: 3.38 kW

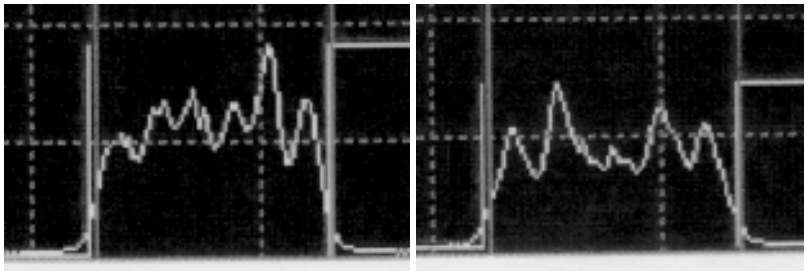

(g) Pumping power: 3.56 kW (h) Pumping power: 3.90 kW

Figure 4.31 Cross-sectional energy distributions at different pumping powers

4.4.1.2 M^2 at Various Aperture Diameters

The beam propagation factor is a function of the size of the intra-cavity mode-control aperture at the pumping power of 3.56 kW, as shown in Table 4.6 and Figure 4.32. It is noted that M^2 values decrease with decreasing aperture diameters from no aperture ($d = \infty$) down to 1.2 mm, approaching the theoretical value of unity 1. However, further reduction in aperture diameter leads to an increase in the M^2 value. This is because the intra-cavity aperture is small enough to cut into the TEM_{00} mode of the stable resonator to a significant extent, causing diffraction effects which deteriorate the beam quality. The calculations using Equations (2.10), (4.27) and (4.29) show that the TEM_{00} beam diameter at the location of the aperture for the system is 1.12 mm in diameter, which falls within the range of the experimental results of 1.0 to 1.2 mm. The sudden deterioration is a clear indication of the onset of a higher-order mode in the laser, as suggested elsewhere with computer simulations inside a stable laser cavity using Huygens integral [2.22].

Table 4.6 M^2 as a function of intra-cavity aperture diameters (the aperture is 145 mm away from the output coupler)

Aperture diameter (mm)	1.0	1.2	1.6	∞
Laser power (W)	1.3	3.4	12.5	47
M^2	2.24	1.10	1.41	5.20

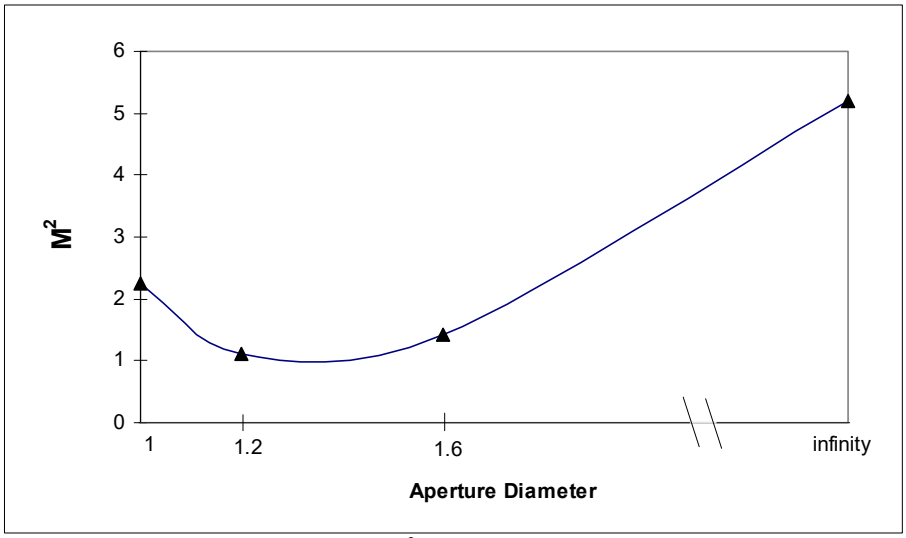

Figure 4.32 M^2 vs. aperture diameter

The observed beam profiles for various intra-cavity apertures are shown in Figure 4.33. The observed beam profiles remain almost unchanged and quasi-Gaussian in character as the laser goes through the transition point ($M^2 \approx 1$). After the transition point, the relative amplitudes of higher-order modes increase with increasing aperture diameters. Because the beam propagation factor for a multimode beam increases with an increase in the fractional power in each mode, it is easy to understand that the beam propagation factors would increase with an increase in aperture diameter without significant diffraction effects. Comparing Figures 4.33(b) and (c), it is found that the distributions are very different because of diffraction. This re-affirms that the transition point lies somewhere near the aperture diameter of ϕ1.2 mm.

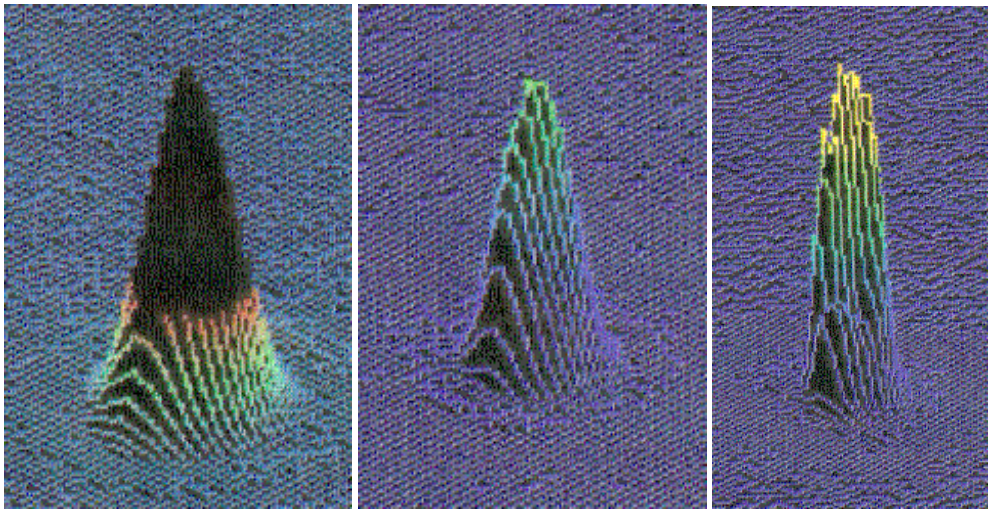

(a) ϕ1.6mm (b) ϕ1.2mm (c) ϕ1.0 mm

Figure 4.33 Laser beam profiles at different intra-cavity apertures

The beam parameters were measured again after the aperture was moved closer to the rear mirror by 35 mm while the other parameters were kept unchanged. The results are shown in Table 4.7. It is found that the transition point is at a smaller aperture diameter compared with previous aperture position where the aperture was placed closer to the output coupler. At the same time, the current set of M^2 values are larger and laser powers higher at the same aperture diameters. The results show that the transition point for M^2 equals 1 is related to the aperture position for a given resonator configuration.

Table 4.7 M^2 as a function of the intra-cavity aperture diameters (the aperture is 35 mm away from the rear mirror)

Aperture diameter (mm)	0.7	1.0	1.2	1.6	No
Beam waist (μm)	154	141	137	188	336
Laser power (W)	1.7	12.5	18	30	47
M^2	1.76	1.19	1.38	2.71	5.20

4.4.1.3 M^2 for Different Resonator Geometries

Typical beam propagation factors for different resonators are shown in Table 4.8, where R_1 and R_2 are radii of curvature of the output coupler and the rear mirror, respectively and symbol "-" means that the mirror is a convex mirror. The equivalent resonator diagram is the same as Figure 4.28, where the aperture diameter and the pumping power are constant at ϕ 1.6 mm and 3556 W, respectively.

Table 4.8 Measured propagation factors for different resonators

Parameter	Combination				
	A	B	C	D	E
R_1 (mm)	-800	-800	flat	flat	-1000
R_2 (mm)	-760	flat	flat	-760	flat
M^2	1.23	2.76	2.07	1.19	2.42
Laser power (W)	8.6	7.8	3.5	1.1	6.0
G parameter	0.65	0.17	0.06	0.24	0.15

The last row in Table 4.8 gives equivalent G parameters for relevant resonators (please refer to Section 4.3) as the G factor indicates whether the resonator is stable.

As shown in Table 4.8, all the G parameters are between 0 and 1, which indicates that all the resonators are stable. The resonator with radii of curvature of -800 mm and -760 mm is the best from the view point of output laser power among these resonators, but the resonator with radius of curvature of -760 mm and flat mirror is the best from the view point of the beam propagation factor M^2. It may not be possible to design a resonator which has the best beam propagation factor and the largest laser power. Incidentally, NEC, the laser supplier, uses Combination A, which is a good compromise between high power output and good-quality laser mode.

4.4.2 Investigation of Second-Harmonic Nd:YAG Laser Beam Quality

4.4.2.1 Basic Equation for Second-Harmonic Generation

Frequency conversion utilises the non-linear optical response of an optical medium in intense radiation fields to generate new frequencies. If Maxwell's equations are solved for a coupled fundamental and its second-harmonic (SH) wave propagating in a non-linear medium, then the ratio of the power generated at the second harmonic frequency to that incident at the fundamental (namely, conversion efficiency η) is given by [4.13]

$$\eta = \frac{P_{2\omega}}{P_{\omega}} = l^2 K \frac{P_{\omega}}{A} \frac{\sin^2(\Delta k l/2)}{(\Delta k l/2)^2} \tag{4.75}$$

where l is the length of the non-linear crystal, K is a constant relative to the fundamental beam and crystal materials, A is the cross-sectional area of the fundamental beam, Δk is the wave number difference (or the phase mismatch), which is given by

$$\Delta k = \frac{4\pi}{\lambda_1}(n_2 - n_1) \tag{4.76}$$

where λ_1 is the wavelength of the fundamental wave, and n_1 and n_2 are the indexes of refraction for the fundamental wave and the doubled frequency, respectively.

For a given wavelength and a given non-linear material, K is a constant. It is observed from Equation (4.75) that the conversion efficiency depends on the length of the crystal, the power density, and the phase mismatch.

4.4.2.2 Second Harmonic Laser Set-up

The second harmonic laser consists of the resonator (rear mirror and output coupler), intra-cavity aperture, Nd:YAG rod, Q-switch, and KTP crystal, as shown in Figure 4.34. The Q-switch and the pumping system for the second harmonic laser are the same as those used in the NEC fundamental-wavelength laser (please refer to Chapter 3). The size of the Nd:YAG rod is ϕ4×100 mm. The KTP crystal is in a type II phase-matched condition, i.e. the polarisation vectors of the two incident beams are orthogonal [4.13]. The KTP size is 4×4×8 mm. The phase-matching angle is 23.3°. The crystal is AR coated for 1.06 and 0.532 μm. The angular acceptance and temperature are sufficiently large that no adjustments of the doubling crystal are necessary once the angle is set [4.23, 4.24].

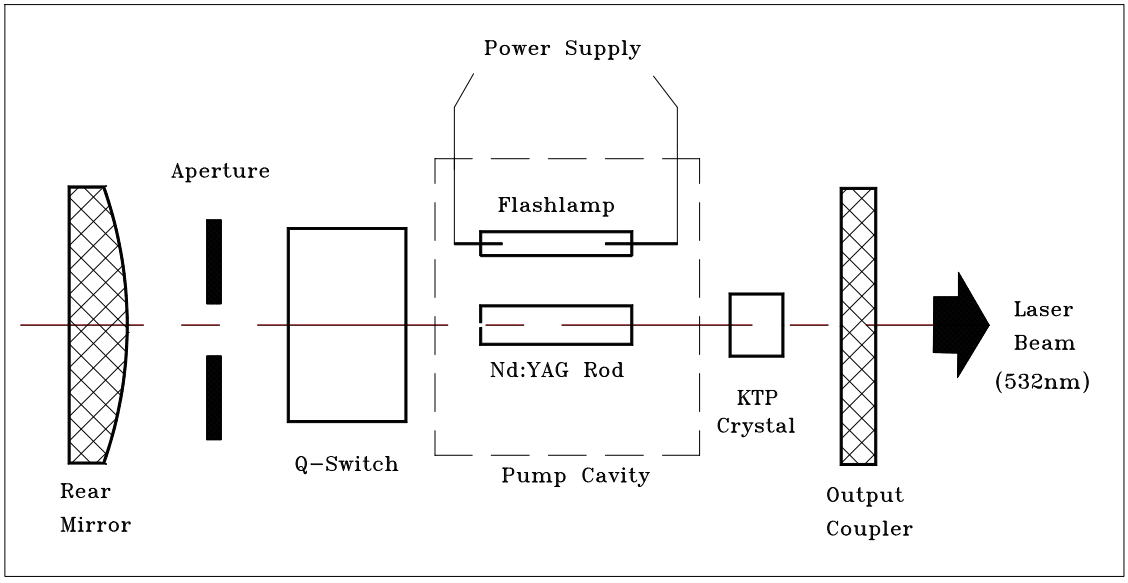

Figure 4.34 Diagram of the second harmonic laser

The cooling of the KTP crystal through a mount is necessary in intra-cavity frequency doubling. The mount can be used to orient the crystal to achieve phase matching and to precisely align the KTP crystal with the optical axis.

The resonator consists of the rear mirror and the output coupler, as shown in Figure 4.34. The specifications of the resonator are as follows:

Rear mirror : Plano-convex
Radius of curvature: 0.5 m or 1 m
Reflectivity: 99.5% @ 1.064 & 0.532 μm

Output coupler : Flat

Reflectivity: 99.5% @ 1.064 μm
Transmission: 99.5% @ 0.532 μm

Resonator length : 670 mm

The apertures used are 1.2 mm or 1.6 mm in diameter. They are cooled by water to maintain the laser power stability.

4.4.2.3 Performance of Second-Harmonic Output Beam

(1) Laser Power

Figure 4.35 shows the second harmonic average laser power as a function of pumping power. The rear mirror has a radius of curvature of 1 m. The aperture is removed, that is, the laser beam has multimode profiles. The experiment shows that the maximum power of 3 W is obtained at the pumping power of 3.56 kW and the Q-switch frequency of 5 kHz.

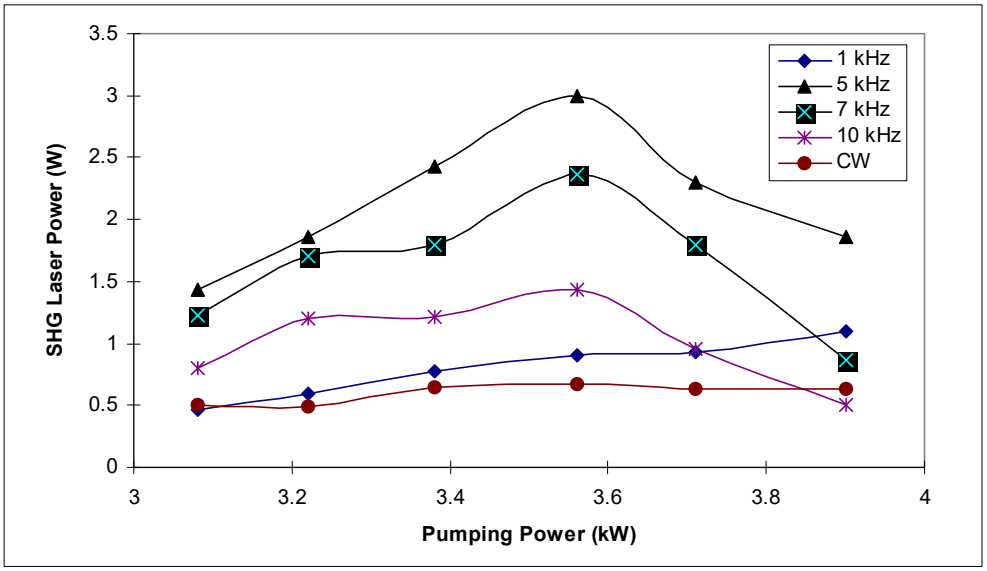

Figure 4.35 Second harmonic laser power vs. pumping power

The change of the average laser power at the Q-switch frequency of 5 kHz in Figure 4.35 is typical. At first, the second harmonic laser power increases with an increase in pumping power, until it reaches the maximum laser power and optimal frequency-doubling conditions. Then, the second harmonic laser power decreases with further increase in pumping power, but the 1.064 μm laser power remains increasing with an increase in pumping power (as shown in Figure 4.36). Note that the cavity configuration for obtaining the output at the fundamental frequency is the one shown in Figure 4.28, with R_1 = -0.8 m and R_2 = -0.76 m, respectively. However, the pulse width becomes wider when the pumping power is increased. For example, the pulse widths of the 1.064 μm beam are 100 ns, 125 ns, and 160 ns, respectively corresponding to the pumping powers of 3.25 kW, 3.43 kW, and 3.58 kW, respectively at the same Q-switch frequency of 5 kHz. Wider pulse width leads to a lower peak power. Another factor is that at higher intensities, the crystal is slightly overdriven and re-conversion of 532 nm radiation to 1064 nm photons starts to become noticeable [4.25]. The other possible reasons for a reduction in laser power of the second harmonic output are lower power density and higher beam divergence when the pumping power is increased.

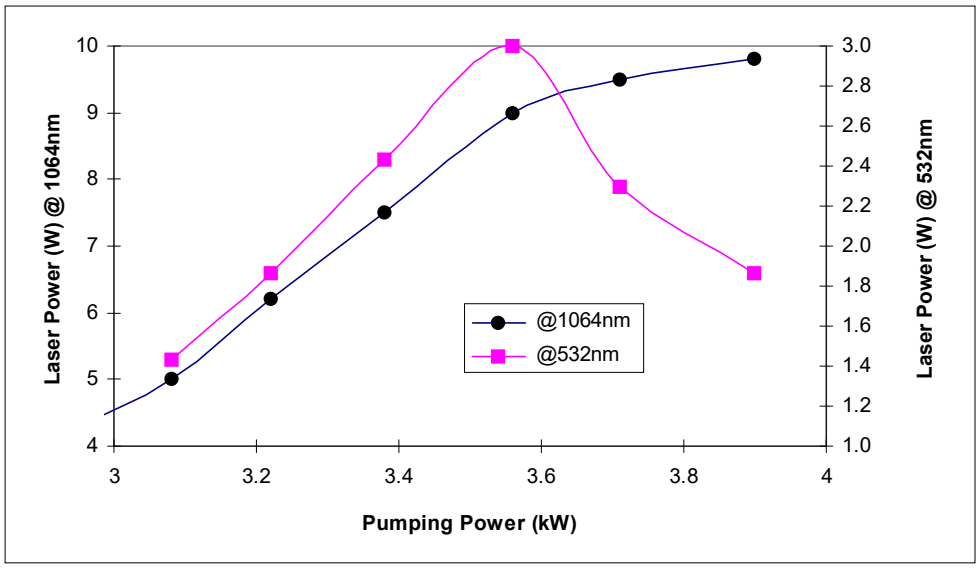

Figure 4.36 Laser powers at 532 nm and 1064 nm as a function of pumping power at a Q-switch frequency of 5 kHz

Figure 4.37 shows the average laser power at the fundamental and frequency-doubled wavelengths as a function of Q-switch frequency. Here the aperture is 1.6 mm in diameter. The pumping power is 3.56 kW. It is obvious that the laser power at the fundamental wavelength increases with an increase in Q-switch frequency, while the laser power at the frequency-doubled wavelength reaches a peak and then drops. The factor resulting in this phenomenon due to the lower conversion efficiency (to be discussed in Section 4.4.2.3(2)).

Figure 4.38 shows the second-harmonic average laser power as a function of pumping power at the aperture of 1.6 mm in diameter. The experiments show that the maximum power of 2.64 W is obtained at the pumping power of 3.71 kW and the Q-switched frequency of 5 kHz (the second harmonic laser power is 2.29 W at the pumping power of 3.56 kW and the Q-switched frequency of 5 kHz). Comparing Figure 4.38 with Figure 4.35, it is seen that the optimal pumping power at the aperture of ϕ1.6 mm is higher than that with no aperture. This is because the loss inside the resonator at the aperture of ϕ1.6 mm is larger. The difference in mode shapes will be discussed later.

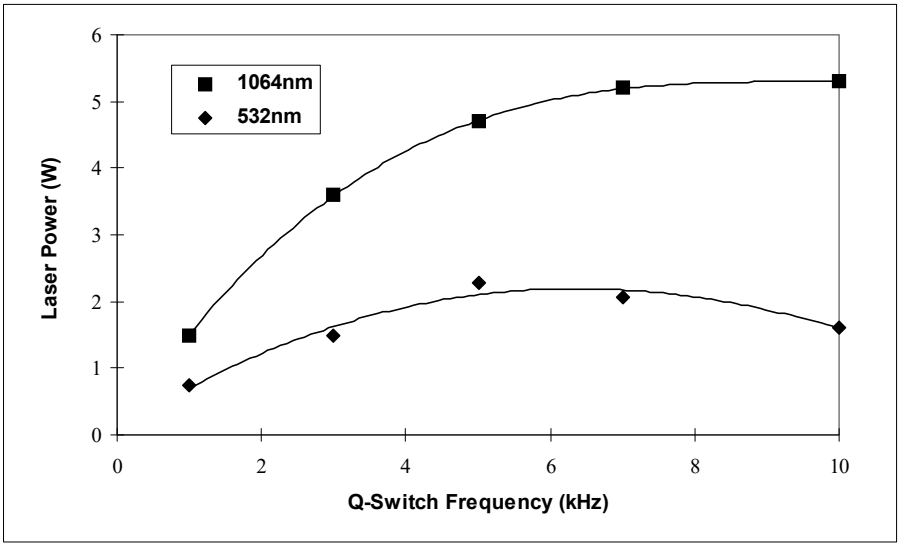

Figure 4.37 Laser powers at 532 nm and 1064 nm as a function of Q-switch frequency at the aperture of ϕ1.6 mm

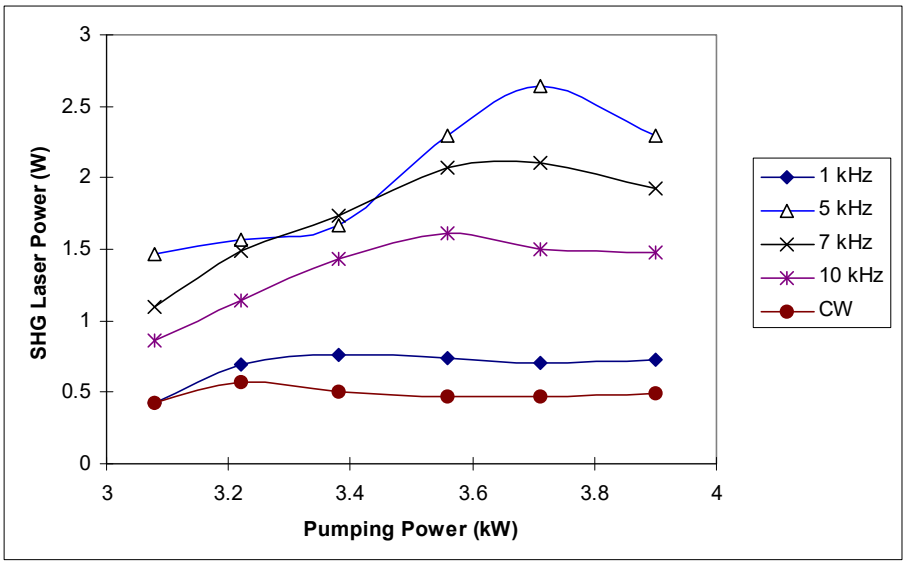

Figure 4.38 Second harmonic laser power
vs. pumping power at the aperture of ϕ1.6 mm

When an aperture of 1.2 mm in diameter is used in the laser, the maximum second harmonic laser power is 1.06 W at the pumping power of 3.56 kW and the Q-switch frequency of 5 kHz.

(2) Conversion Efficiency

Figure 4.39 shows the conversion efficiency as a function of Q-switched frequency at the aperture diameter of 1.6 mm based on the powers shown in Figure 4.37. From Figure 4.39, it is observed that, although the fundamental wavelength laser power at the Q-switched frequency of 1 kHz is only 1.5 W, the peak power is 28.5 kW. Thus, the conversion efficiency at the Q-switch frequency of 1 kHz is high, reaching 48%. After that, the second harmonic laser power and the conversion efficiency increase with increasing Q-switch frequency, until the conversion efficiency reaches the optimal conversion efficiency at the frequency of 5 kHz. After the optimal conversion efficiency, both the second harmonic power and the conversion efficiency decrease with increasing Q-switch frequency. The highest second harmonic laser power of 2.29 W and the optimal conversion efficiency of 48.72% are reached at the Q-switch frequency of 5 kHz. It is observed that the conversion efficiency drops at high frequencies. This is because of the low peak power of the Q-switched pulses. Under CW mode operation, the second harmonic laser power can only achieve 0.065 W, and the conversion efficiency is about 1.1%. Therefore, the peak power is a key factor in achieving high conversion efficiency.

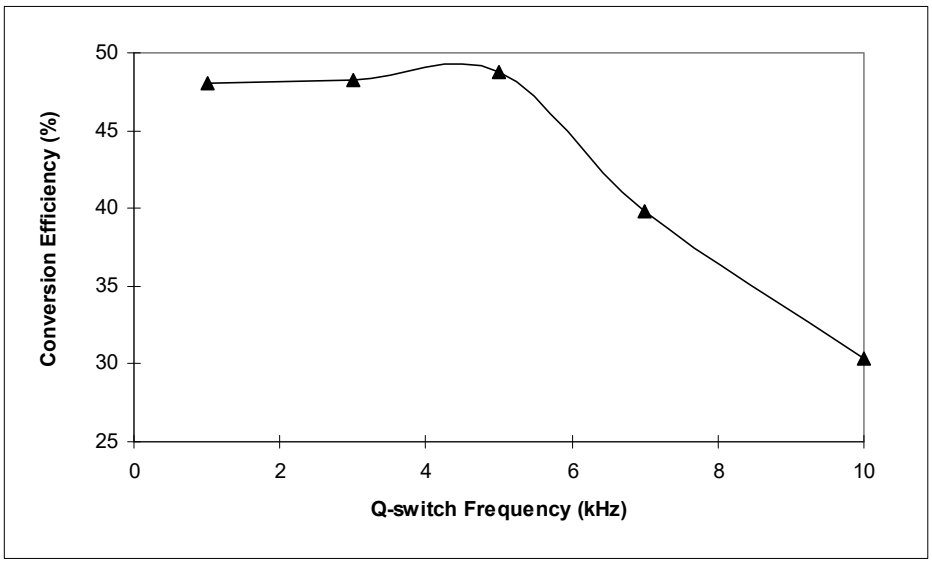

Figure 4.39 Conversion efficiency vs. Q-switch frequency

(3) Beam Propagation Factor

The beam propagation factors (M^2) and other relevant parameters are measured and shown in Table 4.9. The resonator for the second-harmonic laser consists of a plane output coupler and a convex rear mirror with a radius of 1 m. The pumping power and the Q-switch frequency are 3.56 kW and 5 kHz, respectively.

Table 4.9 Second harmonic beam propagation factors and relevant beam parameters

	No aperture	ϕ 1.6 mm	ϕ 1.2 mm
M^2	3.16	2.6	1.17
Measured spot size focused by a lens with f = 133mm (μm)	124	113	90.4
Calculated laser beam waist (mm)	0.55	0.47	0.36
Calculated divergence (full, mrad)	3.88	3.73	2.22
Laser power (W)	3.00	2.29	1.07

The beam energy distributions are shown in Figure 4.40. The distribution looks like a TEM_{00} mode at the aperture of ϕ 1.2 mm, and the distribution without any aperture is multi-mode.

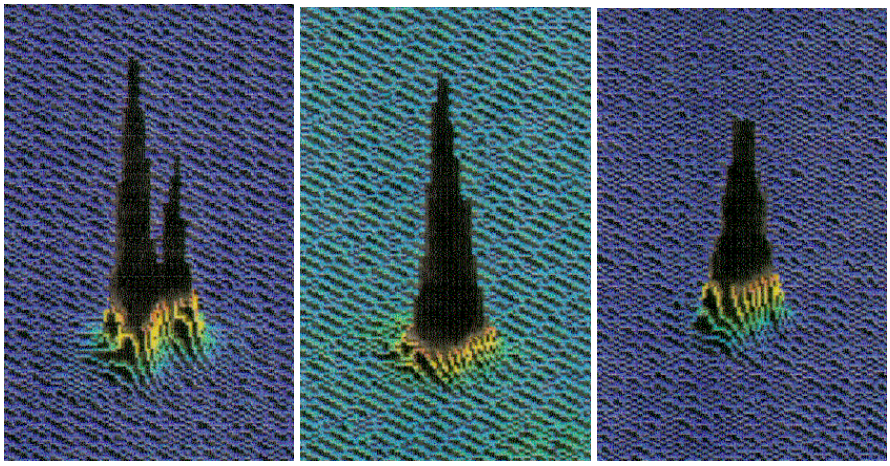

(a) No aperture (b) Aperture ϕ 1.6 mm (c) Aperture ϕ 1.2 mm
Figure 4.40 Laser beam energy distributions at 532 nm

4.5 Summary

The divergence of the probe beam in measuring thermal lensing effect in an optically pumped YAG laser rod has been taken into account in developing the exact formula used to calculate the thermal focal length. The results showed that the thermal focal lengths obtained using the conventional method were shorter than those obtained using the proposed method by 14.3% to 29%. The analyses showed that the proposed calculations are more reasonable and reliable than the conventional calculations. Using a laser beam diagnostic system, experiments performed on a Nd:YAG laser rod confirmed that the thermal lensing effect degraded the laser beam quality.

The resonator stability as a function of the dioptric power of the thermal lens is thoroughly analysed. The resonator in the stability diagram of the (G_1, G_2) plane moves along a straight line, which passes through two stable and three unstable zones. The two stable zones have the same width with respect to the dioptric power. The influence of laser rod position on resonator stability is discussed. The conditions for finding the resonator that is insensitive to the thermal lensing effects are also presented. The results show that the mode volume (or the spot size) in the rod always presents a stationary point. At this point, the output power is insensitive to the fluctuations in the thermal focal length. The thermally insensitive conditions change with rod size, rod positions and radii of the resonator optics. The theoretical results are confirmed by experiments.

A Q-switched Nd:YAG laser system was employed to study the beam quality of the fundamental beam and second harmonic generation. The experiments showed that the beam propagation factor increased with an increase in pumping power, as well as with an increase in intra-cavity aperture diameter. However, the beam quality became worse when the aperture diameter was smaller than the TEM_{00} beam size. Beam propagation factors are mainly determined by the resonator design.

4.5 References:

4.1 H. Weber, “Solid state lasers in the kW average power range”, Proc. of SPIE, Vol. 1839 Solid State Lasers and New Laser Materials (1991), 30-45.

4.2 P. Paugstadt, "Compensation of thermal gradients in repetitively pumped laser rods", Conference on Lasers and Electro-Optics Europe (CLEO'94, Amsterdam, The Nertherlands, Sept. 1994), 307-308.

4.3 D. L. Wright and S. Guggenheimer, "Status of ISO/TC 172/SC9/WG1 on standardisation of the measurement of beam widths, beam divergence, and propagation factor", Proc. of SPIE, Vol. 1834 Laser Energy Distribution Profiles (1992), 2-17.

4.4 B. R. Cai, Y. F. Wang, C. D. Cheng, R. P. Xu, G. H. Wei, Z. X. Zhang, J. H. Liu and G. Q. Mu, Laser Devices, Hunan Science and Technology Publication (1981), 218-219 (in Chinese).

4.5 S. S. Townsend and P. R. Cunningham, "Experimental implications of focal plane behaviour of Gaussian and top-hat beams", Proc. of SPIE, Vol. 1625 Design, Modeling, and Control of Laser Beam Optics (1992), 370-394.

4.6 L. D. Dickson, "Characteristics of propagating Gaussian beams", Applied Optics, Vol. 9, No. 8 (1970), 1854-1861.

4.7 D. C. O'Shea, Elements of Modern Optical Design, John Wiley & Sons, New York, 1985.

4.8 B. K. Zhou, Y. Z. Gao, J. H. Chen and T. R. Chen, Principles of Lasers, Defence Industrial Press, 1980 (in Chinese).

4.9 Y. M. Zhang, Applied Optics: Part I, Mechanical Industry Publications (1982), 35-44 (in Chinese).

4.10 L. Q. Wang and D. Z. Fang, Mathematics Handbook, Advanced Education Publications, Beijing, 1979 (in Chinese).

4.11 W. Koechner, Solid-State Laser Engineering, Springer-Verlag, Berlin (1992), 393-397.

4.12 H. Kogelnik, "Imaging of optical modes-resonators with internal lenses", The Bell System Technical Journal, Vol. 44 (1965), 455-494.

4.13 W. Koechner, Solid-State Laser Engineering, Springer-Verlag, Berlin, 1992.

4.14 H. P. Kortz, R. Ifflander and H. Weber, "Stability and beam divergence of multimode lasers with internal variable lenses", Applied Optics, Vol. 20, No. 23 (1981), 4124-4134.

4.15 S. D. Silvestri, P. Laporta and V. Magni, "Novel stability diagrams for continuous-wave solid-state laser resonators", Optics Letters, Vol. 11, No. 8 (1986), 513-515.

4.16 B. R. Cai, Y. F. Wang, C. D. Cheng, R. P. Xu, G. H. Wei, Z. X. Zhang, J. H. Liu and G. Q. Mu, Laser Devices, Hunan Science and Technology Press, Changsha (1981), 264 (in Chinese).

4.17 W. J. Xia, "Study of dynamic characteristics and beam quality of high power solid state laser", Ph. D. dissertation, Huazhong University of Science and Technology, Wuhan (1995), 20-22 (in Chinese).

4.18 H. Weber, R. Ifflander and P. Seiler, "High power Nd-lasers for industrial applications", Proc. of SPIE, Vol. 650 High Power Lasers and Their Industrial Applications (1986), 92-100.

4.19 V. Magni, "Resonators for solid-state lasers with large-volume fundamental mode and high alignment stability", Applied Optics, Vol. 25, No. 1 (1986), 107-117.

4.20 J. P. Lortscher, J. Steffen and G. Herziger, "Dynamic stable resonators: a design procedure", Optical Quantum Electronics, Vol. 7, No. 5 (1975), 505-514.

4.21 H. J. Zhai, B. Q. Li and C. Chen, "Influence of laser rod position on a thermal insensitive convex-concave resonator", Acta Optica Sinica, Vol. 14, No. 10 (1994), 1026-1030 (in Chinese).

4.22 A. E. Siegman, "Defining and measuring laser beam quality", Solid-State Lasers: New Development and Applications, edited by M. Inguscio and R. Wallenstein, Plenum Press, New York (1993), 13-28.

4.23 W. Koechner, R. Burnham, J. Kasinsiki, P. Bournes, D. DiBiase, K. Le, L. Marshall and A. Hays, "High-power diode-pumped solid state lasers for optical space communications", Proc. of SPIE, Vol. 1522 Optical Space Communications II (1991), 169-179.

4.24 Fujian Castech Crystals, Inc. product catalogue, Potassium Titanyl Phosphate ($KTiOPO_4$, KTP), 1995

4.25 W. Koechner, R. Burnham, J. Kasinski, P. Bournes, D. DiBiase, K. Le, L. Marshall and A. Hays, “High-power diode-pumped solid-state lasers for optical space communications”, Proc. of SPIE, Vol. 1522, Optical Space Communications II (1991), 169-179.